

# Comparison of the Pacific Decadal Oscillation in climate model simulations and observations

Yun Wei,<sup>a</sup>  Haipeng Yu,<sup>a,b\*</sup> Jianping Huang,<sup>a</sup> Yongli He,<sup>a</sup> Bin Yang,<sup>a</sup> Xiaodan Guan<sup>a</sup>  and Xiaoyue Liu<sup>a</sup>

<sup>a</sup> Key Laboratory for Semi-Arid Climate Change of the Ministry of Education, College of Atmospheric Sciences, Lanzhou University, Lanzhou, China

<sup>b</sup> Key Laboratory of Arid Climate Change and Reducing Disaster of Gansu Province, Key Open Laboratory of Arid Climate Change and Disaster Reduction of CMA, Institute of Arid Meteorology, China Meteorological Administration, Lanzhou, China

**ABSTRACT:** The ability of climate models to simulate the Pacific Decadal Oscillation (PDO) and its global teleconnections is examined using the outputs of 20 Coupled Model Intercomparison Project (CMIP5) models from historical experiments. It is shown that the global warming trend is reproduced by the models, but there is a considerable difference between the models in the PDO region. The standard deviation of detrended sea surface temperature anomalies (SSTAs) in the models is similar to that of the observations, especially in the central and eastern equatorial Pacific and the North Pacific, which are the regions closely associated with the PDO and El Niño-Southern Oscillation. The globally averaged SSTA during 1900–1940 in the CMIP5 models and observations showed large divergence, which is mainly due to the SSTA in the PDO region. The most significant cycle of the PDO indexes in most of the models had a 60–80 years period, which is different from the observed PDO period (40–60 years). However, the models perform better for the spatial pattern of the PDO, and 90% of the spatial correlations between the models and observations of the spatial pattern of the PDO are above 0.8. In addition, the models can simulate the basic correlation between the PDO and Pacific SSTA variability, but most of them overestimate the relationship in the Indian and Atlantic Oceans. The CMIP5 models are better at simulating the impact of the PDO on winter precipitation in southern North America but are less accurate in simulating summer precipitation in eastern China. This is probably because most of the models are not accurate in simulating the impacts of the PDO on the western Pacific subtropical high and the East Asian summer monsoon.

KEY WORDS Pacific Decadal Oscillation; climate model simulations; CMIP5; sea surface temperature

Received 28 April 2017; Revised 22 September 2017; Accepted 25 October 2017

## 1. Introduction

The oceans play an important role in the climate system, due in part to their large heat storage capacity; the heat capacity of the surface ocean column (approximately 3.5 m deep) is as large as that of the entire atmosphere (Deser *et al.*, 2010; Shan *et al.*, 2014). The oceans' thermal inertia is communicated to the atmosphere via turbulent and radiative energy exchanges at the sea surface. Sea surface temperature (SST), particularly in the North Pacific Ocean associated with the Pacific Decadal Oscillation (PDO), is closely connected with the internal variability of the climate (Deser *et al.*, 2010; Polade *et al.*, 2013; Dong and Zhou, 2014a). The PDO is commonly defined as the leading empirical orthogonal function (EOF) of the sea surface temperature anomalies (SSTAs) in the North Pacific Ocean [20–70°N, 110°E–100°W], and the PDO index is defined by the normalized time series of the first

principal component (PC1) (Mantua *et al.*, 1997; Zhang *et al.*, 1997; Deser *et al.*, 2010; Lapp *et al.*, 2012; Newman *et al.*, 2012). During the warm phase of the PDO, SSTAs are positive along the western coast of North America and in the tropical Middle and East Pacific and are negative in the central and western North Pacific; the opposite situation occurs during the cool phase of the PDO (Mantua *et al.*, 1997; Newman *et al.*, 2012).

Although the PDO exists in the North Pacific, it can induce widespread impacts at a global scale in the atmosphere, ocean and marine ecosystems (Deser *et al.*, 2010). For example, the Pacific decadal variability plays a significant role in the long-term US summertime drought events (Barlow *et al.*, 2001). Furthermore, several studies have suggested a possible link between the PDO and the decadal variability of the East Asian summer monsoon (EASM) and the associated rainfall changes over East Asia, especially in eastern China (Zhu and Yang, 2003; Ma, 2007; Zhu *et al.*, 2011; Yu *et al.*, 2015; Zhu *et al.*, 2015; Yang *et al.*, 2017). For example, the worst drought conditions since the late 1970s in North China have been reported to be closely connected with the PDO (Ma, 2007). Some recent studies (Zhu *et al.*, 2011; Yu *et al.*, 2015; Zhu *et al.*,

\*Correspondence to: H. Yu, Key Laboratory for Semi-Arid Climate Change of the Ministry of Education, College of Atmospheric Sciences, Lanzhou University, Lanzhou 730000, China. E-mail: hpyu09@lzu.edu.cn

2015; Si and Ding, 2016) also suggest that the change in summer rainfall over East China since the early part of this century has been induced by the phase shift of the PDO. The Aleutian low-pressure system also fluctuates in tandem with the PDO variabilities (Deser *et al.*, 2004), and the tropical belt contracts in the Northern Hemisphere during 1950–1979 with the negative phase of the PDO (Allen *et al.*, 2014). Moreover, the PDO significantly contributes to the rise in the global mean sea level (Hamlington *et al.*, 2013), and the PDO reversal corresponds to dramatic shifts in salmon fishing along the western coast of North America (Mantua *et al.*, 1997). In addition, the El Niño-Southern Oscillation (ENSO) in the tropical Pacific and the PDO also affect each other to influence global climate (Gershunov and Barnett, 1998; Newman *et al.*, 2003; Wang *et al.*, 2008; Xie *et al.*, 2010; Wang *et al.*, 2012b; Hu *et al.*, 2014; Wang *et al.*, 2014b; Nidheesh *et al.*, 2017). Many studies have suggested that the phase change of the PDO is associated with the decadal transition of the internal variability of the climate system, particularly for the recent transition from the accelerated warming period to the warming hiatus period (Kosaka and Xie, 2013; Trenberth *et al.*, 2014; Watanabe *et al.*, 2014; Guan *et al.*, 2015a; Guan *et al.*, 2015b; Huang *et al.*, 2016; Yao *et al.*, 2016; Molteni *et al.*, 2017; Yao *et al.*, 2017). Therefore, a more accurate simulation of the decadal variations in SSTA (particularly those of the PDO) is important mainly for climate predictions and the related regional economic development (Mantua *et al.*, 1997; Mantua and Hare, 2002; Newman *et al.*, 2012; Kumar *et al.*, 2013).

The World Climate Research Program (WCRP) launched the fifth phase of the Coupled Model Intercomparison Project (CMIP5) in September 2008, which has been recognized as an important tool for climate modelling and for the projection of future climate change. At present, CMIP5 has been widely used in historical climate modelling and future projections, and however, a number of issues of concern have been found. For example, the historical changes and future expansion of the global dryland are concerning (Huang *et al.*, 2015; Ji *et al.*, 2015), and the CMIP5 historical simulations of warming pattern are different with observations to some extent (Xie *et al.*, 2016; Huang *et al.*, 2017). The CMIP5 models are good at simulating the long-term climate change trends, like global-averaged surface air temperature (Knutson *et al.*, 2013; Dong and Zhou, 2014b); however, there is considerable uncertainty in the simulation of decadal climate variability patterns, such as Atlantic Multidecadal Oscillation (AMO), which may be due to the poor simulation of SST (Kavvada *et al.*, 2013; Trenberth and Fasullo, 2013; Han *et al.*, 2016). In addition, many studies have shown that CMIP5 shows a significant improvement in simulations of the key climate modes in the Pacific and their associated teleconnections compared to those of the earlier CMIP3, albeit with notable regional deviations from the observations (Oshima and Tanimoto, 2009; Lapp *et al.*, 2012; Newman *et al.*, 2012; Park *et al.*, 2013; Polade *et al.*, 2013; Yim *et al.*, 2013; Dong *et al.*, 2014; Yim *et al.*, 2015). However, the systematic assessment of

PDO simulations from CMIP5 is less common. Taking into account the impact of the PDO on the atmosphere, ocean and marine ecosystem (Shan *et al.*, 2014), we compare the temporal and spatial scales of the PDO and its climate impacts according to both the climate models and observations in order to provide a reliable reference for future changes of the PDO and climate projections.

In this study, the simulation capacity of the climate models with regard to the SST related to the PDO is evaluated for the accuracy of the SST field, the PDO and its climatic impacts. Section 2 introduces the applied models and observations, as well as some of the analytic methods used in this study. In Section 3, we investigate the diversity of the climate models in simulating different aspects of SSTA, particularly those associated with the PDO. Section 4 introduces the temporal and spatial variability of the PDO and its related climate changes, in both climate models and observations. The summary and discussion are provided in Section 5.

## 2. Data and method

In this study, the climate model simulation data sets used are from 20 CMIP5 models (the ‘r1i1p1’ ensemble run was selected for each model, as shown in Table 1) (Taylor *et al.*, 2012). The resolution of each model is listed in Table 1. This study focuses on the assessment of the simulated monthly SST from 1880 to 2005. To verify the climate model simulations, three observed SST data sets are used: The Extended Reconstructed SST version 3b (ERSST v3b; Smith *et al.*, 2008) is a global monthly SST data set on a  $2^\circ \times 2^\circ$  grid derived from the International Comprehensive Ocean–Atmosphere Dataset (ICOADS), Centennial Observation-Based Estimates (COBE) (Ishii *et al.*, 2005) is a global monthly mean SST series with a  $1^\circ \times 1^\circ$  spatial resolution since 1850, and the third version of the Met Office Hadley Centre gridded SST data (HadSST3) (Kennedy *et al.*, 2011) is a monthly global field of SST on a  $5^\circ \times 5^\circ$  grid since 1850. Two observed land precipitation data sets were used. One is the Global Precipitation Climatology Center (GPCC; Schneider *et al.*, 2015) precipitation data set, which has a  $1^\circ \times 1^\circ$  spatial resolution and covers the period of 1901–2015. We also used monthly global land precipitation data from the Climatic Research Unit time-series (CRU TS) 3.23 data set (Harris *et al.*, 2014), covering the period of 1901–2014 with a  $0.5^\circ \times 0.5^\circ$  spatial grid. Monthly geopotential heights and wind velocity since 1948 were taken from the US National Centers for Environmental Prediction/National Center for Atmospheric Research (NCEP/NCAR) Reanalysis (Kalnay *et al.*, 1996). The atmospheric data from the European Centre for Medium-Range Weather Forecasts (ECMWF) reanalysis (referred to as ERA20C; see <http://apps.ecmwf.int/datasets/>) are also used. All of the observations and simulation data sets are first interpolated to a global  $2^\circ \times 2^\circ$  horizontal resolution by bilinear interpolation for comparison.

The climatology of 1961–1990 was selected as the reference climate mean in this study to get SSTA by following

Table 1. Details of the 20 CMIP5 models' 'Historical' simulations used in this study. For each model, we chose the 'r1i1p1' ensemble run.

Reference number	Model name	Modelling group	Resolution(Lon × Lat)
1	BCC-CSM1.1	BCC, China	360 × 232
2	BCC-CSM1.1-M	BCC, China	360 × 232
3	CanESM2	CCCma, Canada	256 × 192
4	CCSM4	NCAR, USA	320 × 384
5	CESM1-CAM5	NCAR, USA	320 × 384
6	CSIRO-Mk3.6.0	CSIRO-QCCCE, Australia	192 × 189
7	FGOAL-S-G2.0	LASG, IAP, China	360 × 196
8	FIO-ESM	FIO, China	320 × 384
9	GFDL-CM3	NOAA GFDL, USA	360 × 200
10	GFDL-ESM2G	NOAA GFDL, USA	360 × 210
11	GFDL-ESM2M	NOAA GFDL, USA	360 × 200
12	GISS-E2-H	NASA GISS, USA	144 × 90
13	GISS-E2-R	NASA GISS, USA	144 × 90
14	HadCM3	MOHC, UK	288 × 144
15	HadGEM2-AO	MOHC, UK	360 × 216
16	HadGEM2-ES	MOHC, UK	360 × 216
17	MIROC-ESM	MIROC, Japan	256 × 192
18	MIROC-ESM-CHEM	MIROC, Japan	256 × 192
19	NorESM1-M	(NCC)Norwegian Climate Centre, Norway	320 × 384
20	NorESM1-ME	(NCC)Norwegian Climate Centre, Norway	320 × 384

the Intergovernmental Panel on Climate Change (IPCC) Fifth Assessment Report (Hartmann *et al.*, 2013). The CMIP5 multi-model ensembles mean (CMIP5 EM) is calculated by the weighted average of the simulated SST from 20 models with an equal weight.

When we calculate the global or regional mean SSTA, the area weighted mean was used as described below by Equation (1) and Equation (2).

$$T^{PDO}(n) = \frac{\sum_{i=1}^{N_{PDO}} T(n, i) \cos \varphi_i}{\sum_{i=1}^{N_{PDO}} \cos \varphi_i} \quad (1)$$

$$T^{\text{global}}(n) = \frac{\sum_{i=1}^{N_{\text{global}}} T(n, i) \cos \varphi_i}{\sum_{i=1}^{N_{\text{global}}} \cos \varphi_i} \quad (2)$$

where  $N_{\text{global}}$  and  $N_{PDO}$  denote the number of grid points over the globe and the PDO region, respectively, and  $\varphi_i$  is the latitude of grid  $i$ .

Many metrics were used to assess the SSTA and PDO characteristics in climate model simulations, including the standard deviation (SD), linear trend of global mean SST, wavelet analysis and EOF. In addition, the pattern correlations were used to evaluate the similarity between the model simulations and observations.

### 3. The variability of global SSTA

The SSTA shows an overall warming but exhibits regional differences under global warming; the warming trend is obvious in the South Atlantic and South Indian Ocean,

especially in the South Atlantic, where the warming rate reaches 2 °C/126 years (Figures 1(a) and (b)). However, for HadSST3 (Figure 1(c)), in addition to the above areas showing warming trends, the Central Pacific also shows significant warming due to the missing values in the HadSST3 data set before 1940. Therefore, the ERSST and COBE data sets are used as the main reference observations to assess the model simulations. In addition, in both ERSST and COBE (Figures 1(a) and b), the high latitudes of the North Atlantic and the southern hemisphere show slight cooling trends, but this is less clear in COBE than in ERSST.

Based on the simulated linear trends of SSTA (Figures 1(d)–(x)), most of the model simulations capture the overall warming trend. However, the SSTA in the North Atlantic has a weak cooling trend in CanESM2, CCSM4, FIO-ESM, GFDL-ESM2M, HadCM3, NorESM1-M and NorESM1-ME, but other models do not simulate this signal. The signs of the trend in the North Atlantic from some of the model simulations are completely contrary to the observations, such as those in BCC-CSM 1.1-M, HadGEM2-AO and HadGEM2-ES. Similar to the trend in the North Atlantic, the SSTA trend in the North Pacific also shows considerable divergences between models. Above 65% (13 of 20) of the models show cooling trends in the North Pacific, including CanESM2, CSIRO-Mk3.6.0, GISS-E2-R and MIROC-ESM, but others show warming trends. The CCSM4, MIROC-ESM and MIROC-ESM-CHEM models show a significant warming in the South Atlantic. All of the models, except BCC-CSM1.1 and BCC-CSM1.1-M, do not simulate a significant warming in the northern Indian Ocean. The spatial correlations of the global SSTA trends in 70% (14 of 20) of the models are above 0.75 with those of ERSST. Comparing the individual models, CMIP5 EM is

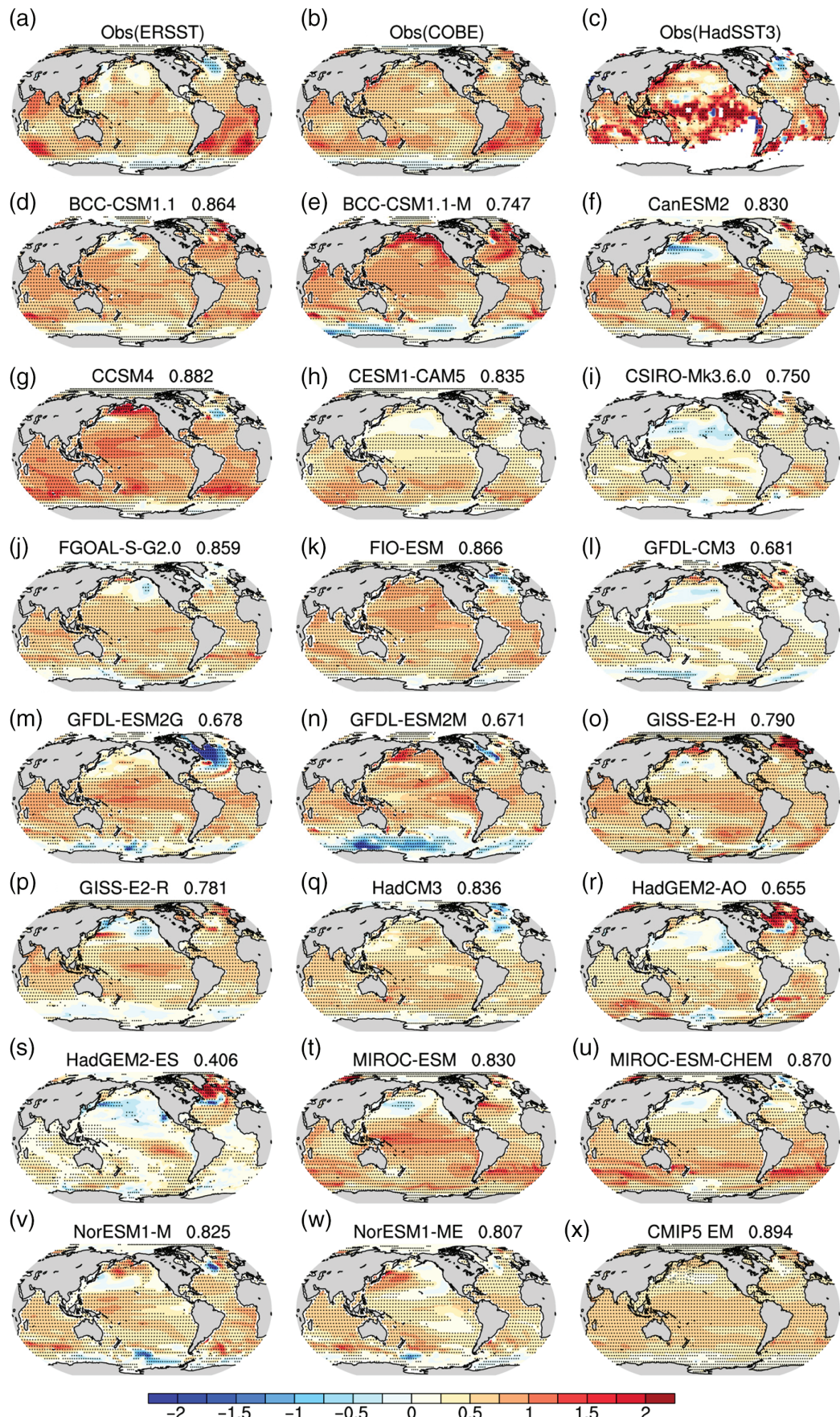


Figure 1. Linear trends of the SSTAs during 1880–2005 in the observations (ERSST (a), COBE (b) and HadSST3 (c)), 20 models (d–w) and CMIP5 EM (x). The unit is °C per 126 years. The spatial pattern correlation of each model with ERSST is given in the right corner. The trend with confidence levels exceeding 95% are denoted with black dots.

most consistent with the observations (the spatial pattern correlation is the largest, 0.894) but does not simulate the regional differences in the warming, and its magnitude is slightly smaller. In general, the models are good for overall global warming, but the SSTA trends in the North Pacific and Atlantic show considerable differences.

After evaluating the SSTA trend, here, we compare the SD of the SSTA in the CMIP5 models to that of the observations (Figure 2). The SD is larger in the central and eastern tropical Pacific, the North Pacific, the North Atlantic and the South Atlantic (Figures 2(a)–(c)), consistent with earlier studies (Bhaskar *et al.*, 2014). The SSTA in these regions, where the PDO, AMO and ENSO occur, is closely connected with the global climate variations on seasonal and longer time scales. The most pronounced area is in the central and eastern equatorial Pacific, where the amplitude of the SD can reach 0.7 °C or above, followed by the North Pacific, where the amplitude of the SD can reach 0.5 °C or above.

Almost all models capture the SD of the SSTA in the tropical central and eastern Pacific and in the North Pacific (Figures 2(d)–(w)). The SD of the SSTA in the tropical central and eastern Pacific in BCC-CSM1.1 (Figure 2(d)), CESM1-CAM5 (Figure 2(h)), and GISS-E2-R (Figure 2(p)) are below 0.9 °C, and the distribution of the large SD area is consistent with the observations, but the other models have poor simulations of the distribution of the SD in the equatorial central and eastern Pacific, where the SD is much greater than 0.9 °C. Furthermore, the amplitudes of the SD of the SSTA in the North Pacific from FGOAL-S-G2.0, FIO-ESM, GISS-E2-H, MIROC-ESM and MIROC-ESM-CHEM models are comparable to the observations, while the other models overestimate this value, particularly GFDL-ESM2G, GFDL-ESM2M and HadGEM2-ES. For the North Atlantic, all models, except for GISS-E2-H, NorESM1-M and NorESM1-ME, simulated the large SD of the SSTA, but the simulations show the overall overestimated amplitude of the SD. All of the spatial correlation coefficients between the models and observations are greater than 0.9 (due to all SDs being positive), among which 40% (8 of 20) of the coefficients are above 0.94, including those of CCSM4, CESM1-CAM5, FGOAL, FIO-ESM, HadGEM2-AO, HadGEM2-ES, NorESM1-M and NorESM1-EM. Most of the models overestimated the SD of the SSTA in the North Pacific, North Atlantic and tropical central and eastern Pacific.

We further compare the global and regional SSTA time series in the CMIP5 simulations and those of the observations (Figure 3). The global averaged SSTAs in the three observations (HadSST3, COBE and ERSST) have a consistent decadal variation, such as the downward trend during 1880–1910, upward trend during 1910–1945, zero trend during 1945–1975 and upward trend during 1975–2005 (Figure 3a). The globally averaged SSTA in 2005 has increased by approximately 0.6 °C compared to that of 1880 (0.56 °C and 0.63 °C in ERSST and COBE, respectively, statistically significant at the 95% level). The global averaged SSTAs from CMIP5 EM are very similar

to the observations during 1880–1900 and 1940–2005, but are obviously higher over 1900–1940. Moreover, the global average SSTA from the CMIP5 EM has a tendency to increase during the whole period of 1880–2005, and the warming trend accelerates after 1964. However, the global averaged SSTAs during 1900–1940 from CMIP5 EM and the observations show considerable divergence, and the CMIP5 EM poorly captures the cooling trend of the SSTA before 1910.

To explore which piece of the ocean dominated the large differences before 1940 between the models and observations, we compare the regionally averaged SSTA time series of 5 major regions using 20 models and two observations (Figures 3(b)–(f)). The SSTAs of the North Atlantic (Figure 3(b)) and the North Pacific (Figure 3(c)) in the observations show a clear downward trend between 1880 and 1910 and are almost the same throughout the period 1880–2005, as is the global trend (Figure 3(a)). However, like the global SSTAs before 1940, the SSTAs in these two regions in the CMIP5 models also show great divergences from the observations. The SSTA in the equatorial eastern Pacific (Figure 3d) has significant interannual variability and an amplitude of approximately 1–2 °C, while the warming trend is weaker. For the Indian Ocean (Figure 3e) and the Arctic Ocean (Figure 3f), the SSTA shows a trend of continuous warming, but the warming trend in the Indian Ocean is far greater than that in the Arctic Ocean. In contrast to Figure 3a, the difference in the globally averaged SSTA in the CMIP5 models and observations is mainly concentrated in the period 1900–1940 and is mainly due to the SSTAs in the PDO and AMO regions among the five regions we chose, although the SSTA in the PDO region is dominant. The PDO is the dominant mode of the SSTA in the PDO region and has been connected both to other parts of the climate system and to impacts on natural resources and marine and terrestrial ecosystems (Newman *et al.*, 2012). Therefore, in the following sections, we examine the variability and climatic impacts of the PDO using CMIP5 models.

#### 4. The model performance of the PDO and its climatic impacts

Following some previous studies (Mantua *et al.*, 1997; Zhang *et al.*, 1997; Newman *et al.*, 2012; Wang *et al.*, 2012a), the monthly PDO index in this study is defined as the standard PC1 from an EOF analysis of monthly detrended SSTAs in the PDO region [20–50°N, 110°E–100°W]. The monthly detrended SSTAs are the difference between the observed monthly SSTA and the monthly mean global average SSTA (Zhang *et al.*, 1997). The PDO index in this study is the annual mean PDO index.

##### 4.1. Temporal and spatial variability of the PDO

The warming hiatus in recent years is closely related to the phase change of the PDO (Guan *et al.*, 2015a; Guan *et al.*, 2015b; Huang *et al.*, 2016; Molteni *et al.*, 2017),

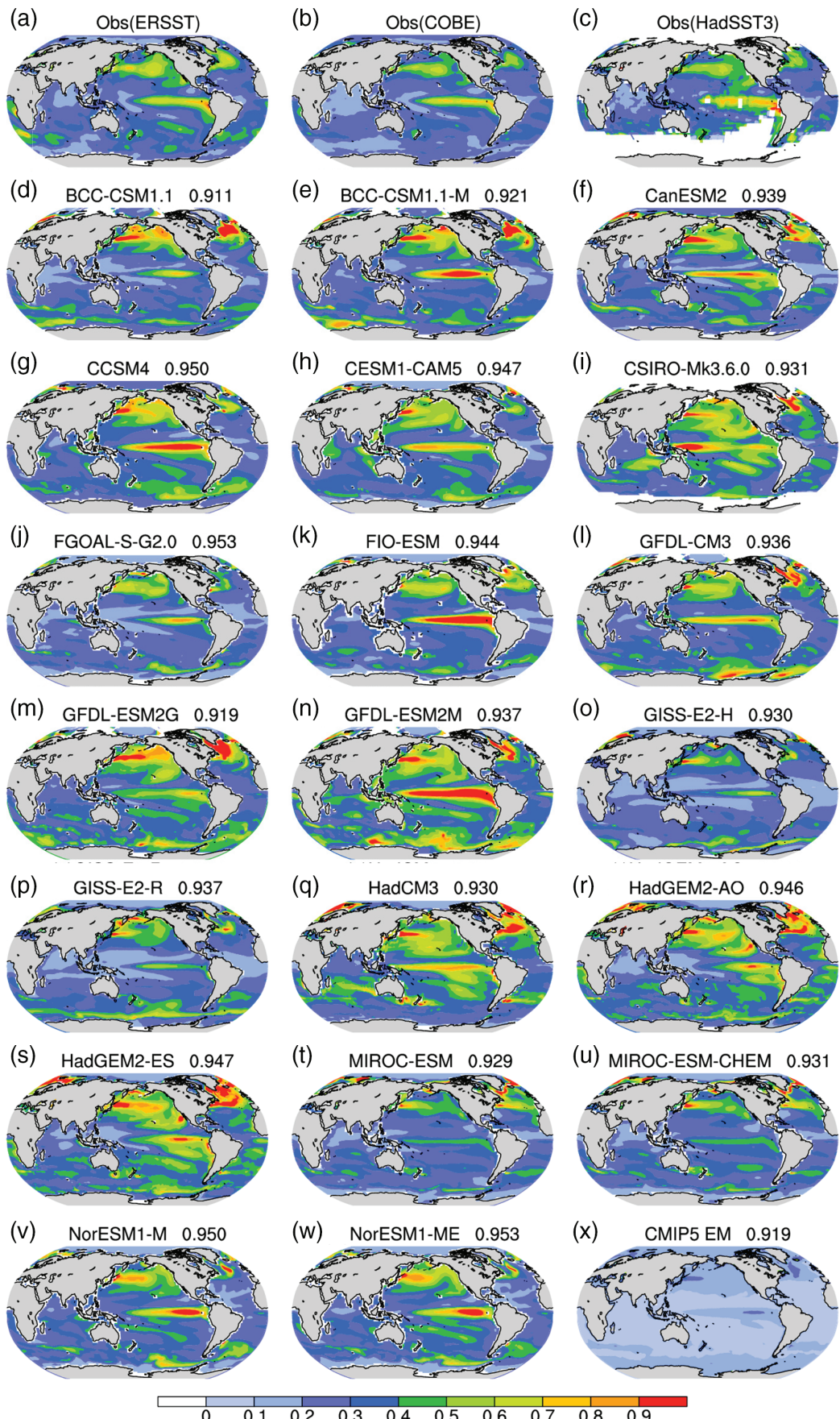


Figure 2. Spatial pattern of the SD of the detrended SSTA (1880–2005) in the three observational data sets (ERSST (a), COBE (b) and HadSST3 (c)), 20 models (d–w) and CMIP5 EM (x). The spatial pattern correlation of each model with ERSST is given in the right corner.

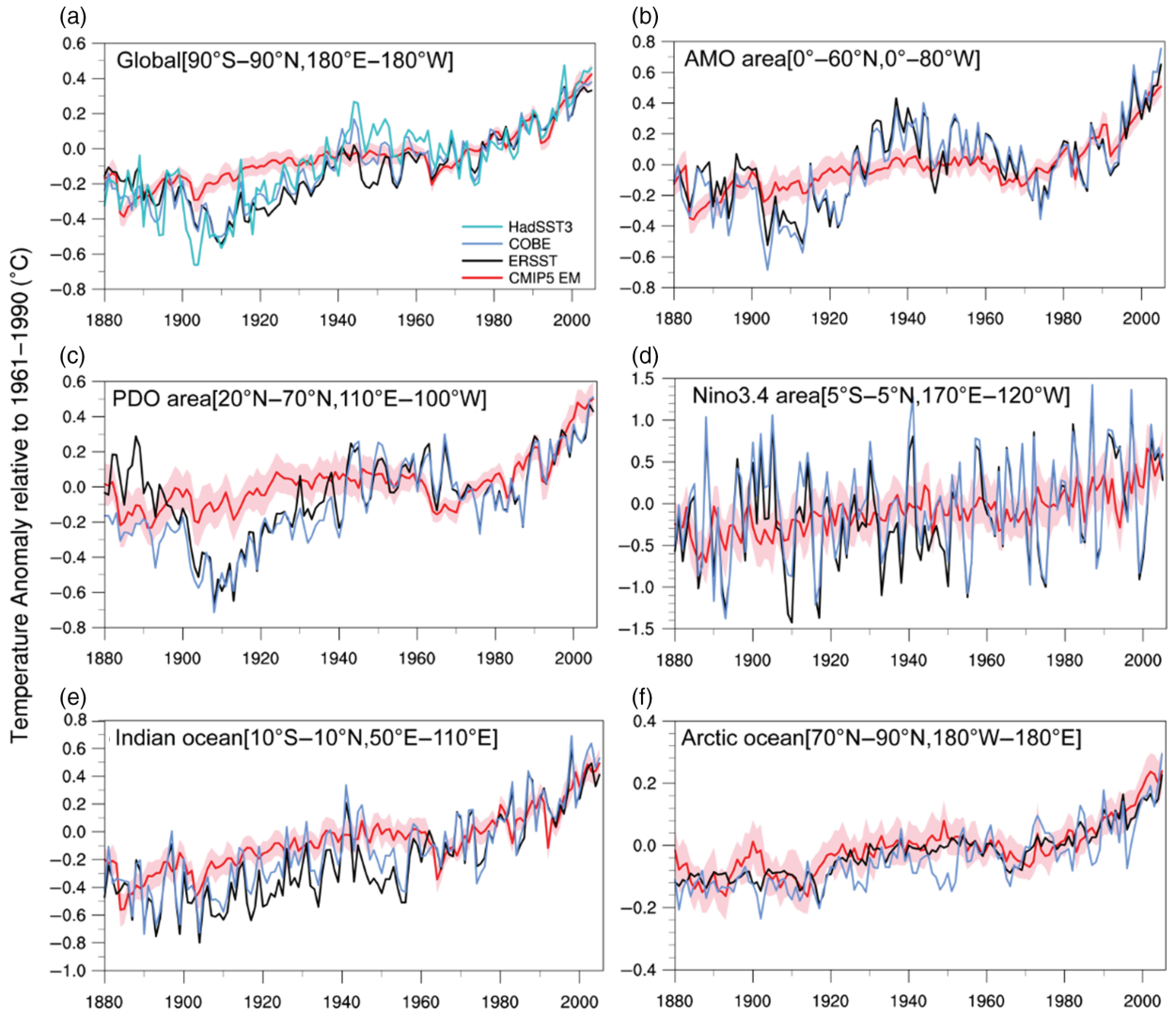


Figure 3. Time series of the annual mean SSTA globally and for the five major ocean regions from the observations and the ensemble mean of CMIP5 models. (a) Global averaged annual SSTA from the ERSST (black line), HadSST3 (light blue line), COBE (dark blue line) data sets and the ensemble mean (red line) from the 20 CMIP5 models. (b–f) are the same as (a) but for the AMO area, PDO area, Nino3.4 area, Indian Ocean and Arctic Ocean, respectively. The red shading denotes the 95% confidence intervals for the 20 models.

which may have important significance for future air temperature. Here, we provide the variations in the PDO index from three observations and 20 CMIP5 models (Figure 4). The PDO has a significant decadal variation, with positive (1896–1910, 1925–1945 and 1976–2004) and negative phases (1911–1925 and 1945–1976). Comparing the PDO indexes of 20 CMIP5 models with the ERSST data set, because the PDO index is normalized, the amplitudes of the PDO indexes in the 20 models are similar to the observations but with random phases. This indicates that the PDO may be largely forced by internal variability. The two best models for the simulation of the PDO index are BCC-CSM1.1 and GFDL-ESM2G, and their correlation coefficients with the ERSST PDO index are 0.303 and 0.191 (statistically significant at the 95% level), respectively.

Wavelet analysis was used to assess the period of the PDO indexes in the model simulations (Figure 5). The results suggested that the observed PDO index has

quasi-20-year, quasi-40-year and quasi-60-year cycles (Figures 5(a)–(c)), which is consistent with many previous studies (e.g., Mantua and Hare, 2002; Macdonald and Case, 2005; Yu *et al.*, 2015; Zhang and Delworth, 2016). With the exceptions of CESM1-CAM5, CSIRO-Mk3.6.0, GFDL-ESM2G and GISS-E2-R, the models underestimate the quasi-40-year cycle of the PDO. Most models can accurately simulate the quasi-20-year periodic oscillations such that they are comparable to those of the observations. The PDO index has a quasi-30-year period in BCC-CSM1.1, CCSM4, GFDL-ESM2M, HadCM3, HadGEM2-AO and NorESM1-M, which is not reflected in the three observations. Except for CanESM2, CCSM4, FIO-ESM and NorESM1-M, the most significant cycles of the PDO index in models are 60–80 years, which is different from those of the ERSST and COBE observations (40–60 years).

Furthermore, the spatial features of the PDO in the models are assessed by comparing them with the observations

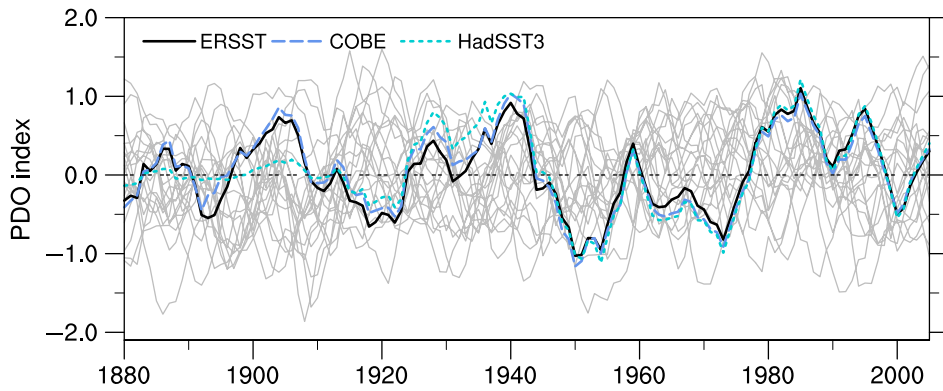


Figure 4. The 5-year running mean PDO index from the ERSST (black solid line), COBE (dark blue dashed line) and HadSST3 (light blue dot line) data sets and 20 CMIP5 models (grey lines). [Colour figure can be viewed at [wileyonlinelibrary.com](http://wileyonlinelibrary.com)].

(Figure 6). As in many previous studies (Mantua *et al.*, 1997; Newman *et al.*, 2012), the spatial pattern of the PDO is defined by the leading EOF (approximately 25% variance) of the SSTA in the North Pacific, which corresponds to negative SST anomalies in the central and western North Pacific and positive anomalies along the eastern coast in ERSST and COBE (Figures 6(a) and (b)) for a positive phase (Figures 6(a)–(c)). However, in HadSST3, the intensity of the negative centre is weaker, while the intensity of the positive value over the eastern Pacific coast is stronger.

Figures 6(d)–(w) show the spatial pattern of the PDO for each CMIP5 model. In addition to BCC-CSM1.1, GISS-E2-H, GISS-E2-R, HadCM3, HadGEM2-AO, HadGEM2-ES and MIROC-ESM, the range of the EOF1 interpretation variances by most of the models (20.0–30.4%) are comparable to that of the observations (21.6–26.4%). The spatial correlation is above 0.8 (approximately 0.7–0.95) for all models with the observation (Figures 6 and 7). In addition, the root mean square error (RMSE) of these models and the observation are small (0.01–0.03) and the SD of the observations and the 20 models are approximately 0.03, which is close to the observations (Figure 7). Except in GFDL-CM3 and HadGEM2-AO, the negative centre positions of the PDO spatial pattern in all models are too west relative to in observations (Figure 6). Among the 20 models, the PDO mode is best captured by FIO-ESM, GFDL-CM3 and HadGEM2-AO (points 8, 9 and 15 in Figure 7, respectively). The results indicated that the models are able to simulate the spatial pattern of the PDO better than the PDO index.

#### 4.2. PDO impacts

##### 4.2.1. The relationship between SSTA and PDO

As stated in Section 2, the SSTA in the PDO region may be the dominant factor for the huge divergence of the global average SSTA before 1940 found by the climate models and observations. We further compare the spatial patterns of the correlations found by the PDO index and the SSTA in the models and observations (Figure 8). Similar to the PDO pattern in the Pacific (Figure 6), the patterns

show a negative correlation in the North Pacific and the western South Pacific and a positive correlation in the equatorial Pacific, extending to the western equatorial Pacific. As many of the climate anomalies associated with the PDO are broadly similar to those connected with ENSO variations (Mantua *et al.*, 1997; Wang *et al.*, 2014b), the spatial pattern of the correlation between the PDO index and the SSTA suggests a link between the SSTA variability in the extratropics and the tropics via changes in the atmospheric circulation (Oshima and Tanimoto, 2009). In addition, the SSTA in the central Indian Ocean shows a significant positive correlation with the PDO index, while in the northern Indian Ocean, ERSST shows a positive correlation with the PDO index that is not obvious in COBE. The SSTA in the Atlantic subtropical region shows a positive correlation with the PDO index in the ERSST data, which is similar in COBE and HadSST3.

Compared to the observations, CCSM4, CESM1-CAM5, HadGEM2-AO and HadGEM2-ES well model the correlation between the Pacific SSTA and PDO index (Figures 8(d)–(w)). The spatial patterns in the above models are also the most similar to the ERSST observations, and the spatial pattern correlations between them and ERSST are 0.796, 0.792, 0.827 and 0.764, respectively. For the Indian Ocean, GFDL-ESM2G, HadCM3 and HadGEM2-ES show a weak positive correlation between the SSTA in the northern Indian Ocean and the PDO index, which is similar to observations. However, there are some differences in the spatial correlation patterns between the PDO index and the SSTA in BCC-CSM1.1, FGOAL-S-G2.0, GISS-E2-H and GISS-E2-R, which may indicate that they do not model the PDO mode well (Figure 6). In general, the models can simulate the basic correlation between the PDO and Pacific SSTA variability, but most of them overestimate the relationships in the Indian and Atlantic Oceans.

##### 4.2.2. The impact of the PDO on precipitation

The PDO plays an important role in precipitation over eastern China and North America (Mantua *et al.*, 1997; Barlow *et al.*, 2001; Mantua and Hare, 2002; Chan and Zhou, 2005; Shen *et al.*, 2006; Ma, 2007; Zhu *et al.*, 2011; Yu,

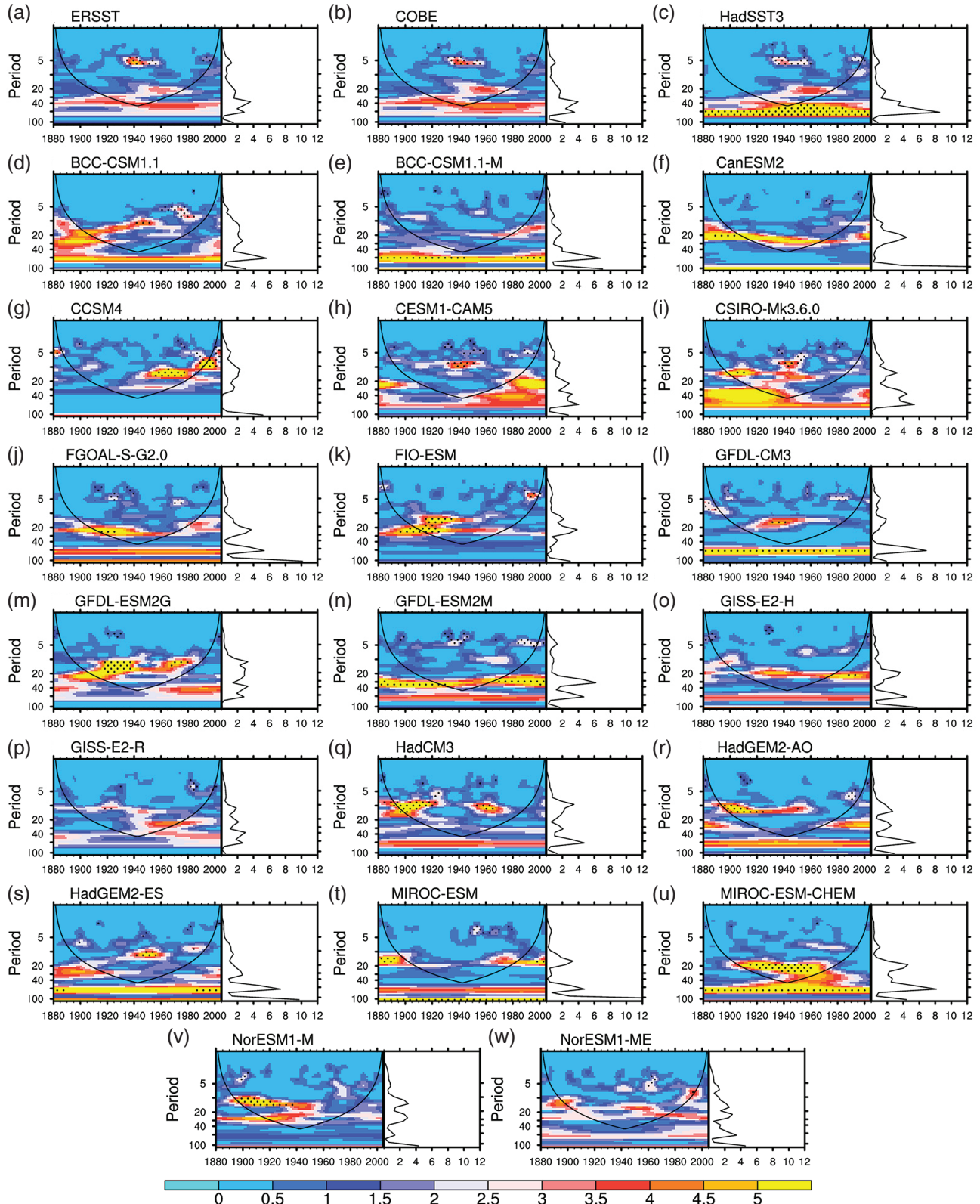


Figure 5. Wavelet analysis of the PDO index for the observations (ERSST (a), COBE (b) and HadSST3 (c)) and 20 models (d–w). The left side of each panel represents the wavelet power spectrum, using the Morlet wavelet. The x-axis is the wavelet location in time and the y-axis is the wavelet period in years. The black line is the cone of influence and the regions with black dots are the 95% significance regions, using the red-noise background spectrum. The right side of each panel represents the wavelet power spectrum intensity. The x-axis is the spectrum strength at each period.

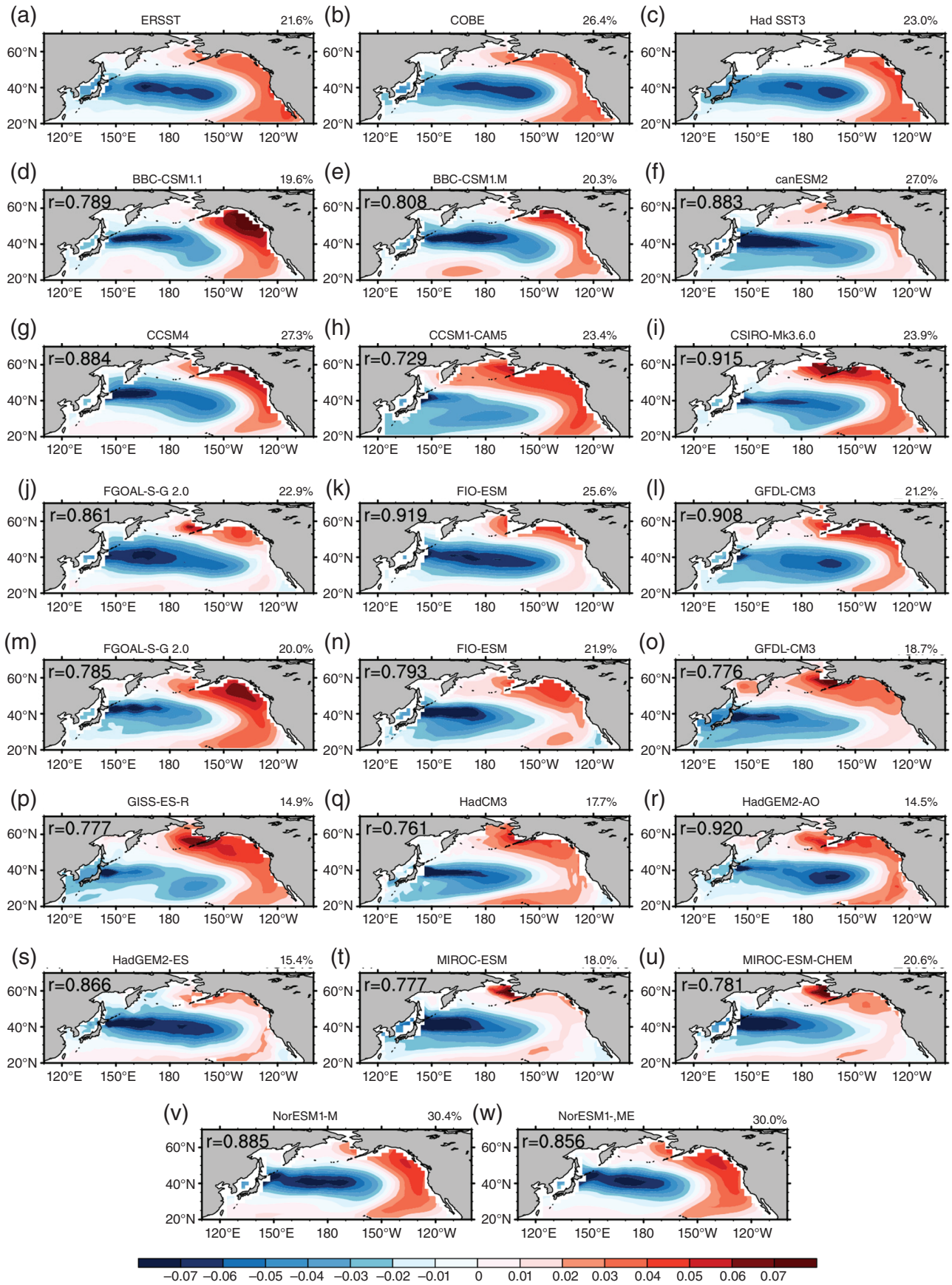


Figure 6. The PDO spatial pattern (the leading EOF of the North Pacific SSTs) in the three observational data sets (ERSST (a), COBE (b) and HadSST3 (c)) and models (d–w). The explained variance of the leading EOF is given in the right corner. The  $r$  in d–w represents the spatial pattern correlation of each model with ERSST.

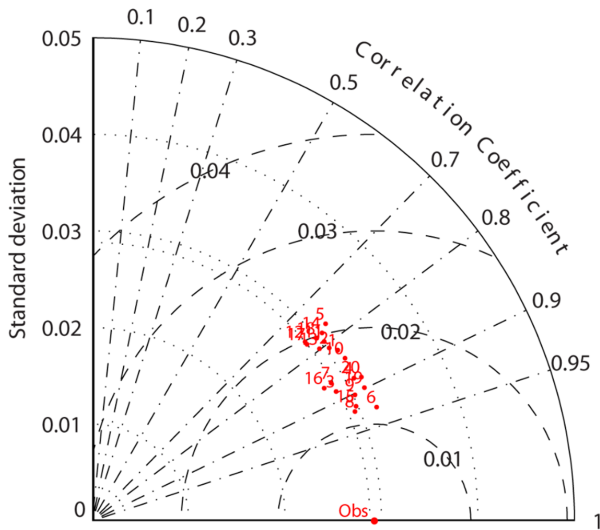


Figure 7. Taylor diagram showing the spatial features of the regressions displayed in Figure 6. Obs and 1–20 represent ERSST and the CMIP5 models, as listed in Table 1, respectively. The distance of any point from the origin indicates SD of time series, the distance of any point from the Obs reference point indicates the centred root mean square (RMS) difference between each model or ensemble mean and observation. Correlation between each model or ensemble mean and observation is given by the azimuthal coordinate. The best models will fall closest to the observational point where the RMS error approaches zero and approaches that of the observations and the correlation approaches one (Taylor, 2001). [Colour figure can be viewed at [wileyonlinelibrary.com](http://wileyonlinelibrary.com)].

2013; Chylek *et al.*, 2014; Yu *et al.*, 2015; Zhu *et al.*, 2015; Si and Ding, 2016; Yang *et al.*, 2017). Here, we first focus on the regression pattern of the summer precipitation onto the observation-based PDO index and 20 CMIP5 climate models over eastern China (Figure 9). Because the PDO is a largely decadal oscillation, an 11-year running average was performed to extract the decadal variability of the precipitation (Figures 9 and 12). In comparing the two observations (Figures 9(a) and (b)), the warm phases of the PDO tend to coincide with the large positive precipitation anomalies in the middle and lower Yangtze River Valley (YRV) and the negative anomalies in both North and South China. The opposite moisture precipitation regimes exists during cool phases. Some studies (He and Gong, 2002; Guo *et al.*, 2004; Yu *et al.*, 2015) have indicated this pattern is a result of changes in the strength of the summer monsoon and the subtropical high altered by the PDO. During the warm phases of the PDO, the summer monsoon is weak, and the strong western Pacific subtropical high (WPSH) is located far to the south and west (He and Gong, 2002; Guo *et al.*, 2004). There is a negative correlation ( $-0.72$ ) between the PDO and decadal EASM variability (Wang, 2002), but a positive correlation ( $0.78$ ) between the PDO and decadal WPSH variability (defined as the mean summer 500 hPa geopotential height anomalies averaged over  $20\text{--}25^\circ\text{N}$  and  $125\text{--}140^\circ\text{E}$ ) (Figure 10(a)). As referenced in some previous studies (Hu, 1997; Gong and Ho, 2002; Zhou and Yu, 2005; Ding *et al.*, 2008; Zhou *et al.*, 2009a; Zhou *et al.*, 2009b), the strengthening of the WPSH is primarily responsible for an increase in precipitation

over the YRV region and the weakening of the EASW contributing to a decrease in precipitation over North and Northeast China (Figure 11). During the warm phases of the PDO, the weakening of the EASW and the strengthening of the WPSH both lead to a decrease in summer precipitation in North China, but an increase in summer precipitation in the YRV region.

When compared to observations, it is evident that FGOAL-S-G2.0, GFDL-CM3, HadGEM2-ES and MIROC-ESM-CHEM are better at simulating the correlations between the summer precipitation in Eastern China and the PDO index (Figures 9(c)–(v)). However, for FIO-ESM, GISS-E2-H and NorESM1-M, the patterns of summer precipitation related to the PDO are basically the opposite of those observed. The GFDL-CM3 captures the obvious positive/negative correlations between the PDO and the WPSH/EASW (Figure 10b), and it is the best model to simulate the impacts of the PDO on summer precipitation in eastern China. In addition, the spatial pattern correlations between the PDO and summer precipitation over eastern China in most of the models are quite small, such as the BCC-CSM1.1-M, CCSM4, CESM1-CAM5, GFDL-ESM2G, GFDL-ESM2M and NorESM1-ME. This may be because these models cannot capture the impacts of the PDO on the WPSH and EASW. For example, CESM1-CAM5 and GFDL-ESM2G do not capture the positive (negative) correlation between the PDO and the WPSH (EASW) (Figure 10(b)). In addition, for CCSM4, although it captures the strengthening WPSH during the warm phases of the PDO, which leads to more summer precipitation in YRV region, it presents a positive correlation between the PDO and the EASW, which leads to more summer precipitation in North China. For the GISS-E2-R, HadCM3, HadGEM2-AO and HadGEM2-ES, the summer precipitation over North China tends to decrease coinciding with the warm phases of the PDO, which is consistent with observation. This may be due to the weakened EASW induced by the warm phases of the PDO in these models, which leads to less summer precipitation over North China. In general, approximately 40% of the spatial pattern correlations of the pattern of summer precipitation influenced by the PDO between models and observations are negative.

In addition, the winter precipitation anomalies in southern North America are typically linked to PDO variations (Mantua *et al.*, 1997; Cayan *et al.*, 1998; Brown and Comrie, 2004; Kurtzman and Scanlon, 2007) and it tends to increase coinciding with the warm phases of the PDO (Figure 12a, b). The winter 700 hPa geopotential height anomaly over the southern North America region [ $20\text{--}30^\circ\text{N}$ ,  $110\text{--}95^\circ\text{W}$ ] is negatively related ( $-0.31$ ) with the PDO index during the period of 1948–2005 (Figure 14a). When the PDO is in its warm phase, a deep and significant cyclonic circulation anomaly is observed with a negative correlation of geopotential height with PDO index in the North Pacific at both 700 hPa and 500 hPa, which contributes to the transport of moisture from the Pacific to the west coast of North America, especially at 500 hPa (Figure 13). Meanwhile, there also

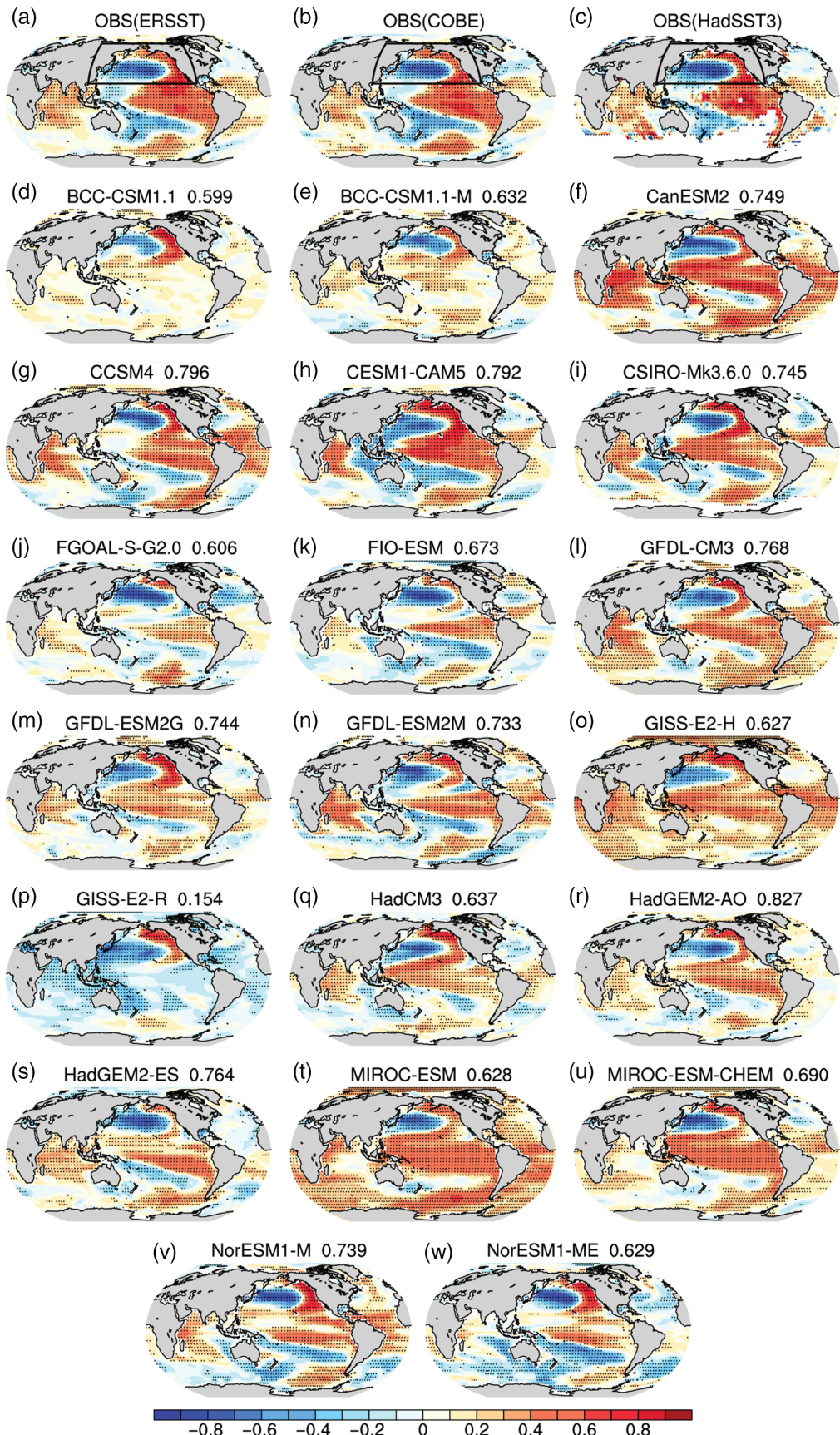


Figure 8. Spatial pattern of the correlation between SSTA (1880–2005) and the PDO index for the observations (ERSST (a), COBE (b) and HadSST3 (c)) and models (d–w). The PDO indexes in a–c are from the ERSST data set, and the PDO indexes in d–w are from the respective model. Black dots indicate statistical significance at the 95% confidence level based on Student's *t*-test. The spatial pattern correlation between the pattern of each model and ERSST is given in the right corner. The black squares in a–c represent the PDO region.

COMPARISON OF THE PDO IN CLIMATE MODEL SIMULATIONS AND OBSERVATIONS

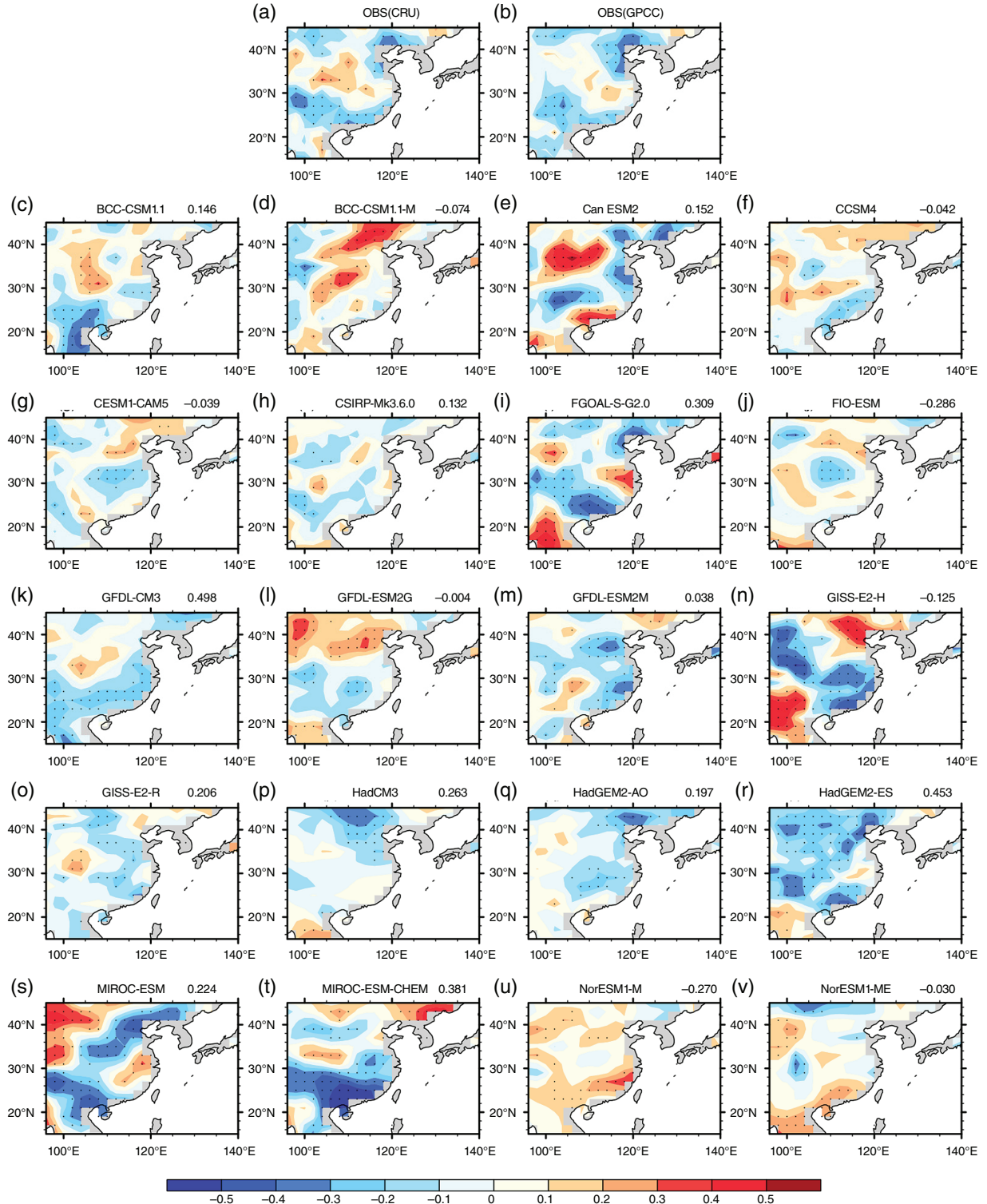


Figure 9. Spatial pattern of the correlation between 11-year running mean summer precipitation anomalies over eastern China (1901–2005) and the PDO index for the observations (CRU (a) and GPCC (b)) and models (c–v). The PDO indexes in a–b are from the ERSST data set, and the PDO indexes in c–v are from the respective model. Black dots indicate statistical significance at the 95% confidence level based on Student's *t*-test. The spatial pattern correlation of the pattern in each model and CRU is given in the right corner.

exists a cyclonic circulation along with a negative correlation of geopotential height in south Northern America, which is beneficial to the enhancement of precipitation in the area. The enhanced west wind near the west coast of southern North America further contributes to the

transport of water vapour to the western part of southern North America. In such a circulation anomaly in the warm phase of PDO, adequate water transport eventually manifests the winter precipitation in the area (Figure 13). Except for BCC-CSM1.1-M and NorESM1-M, most of

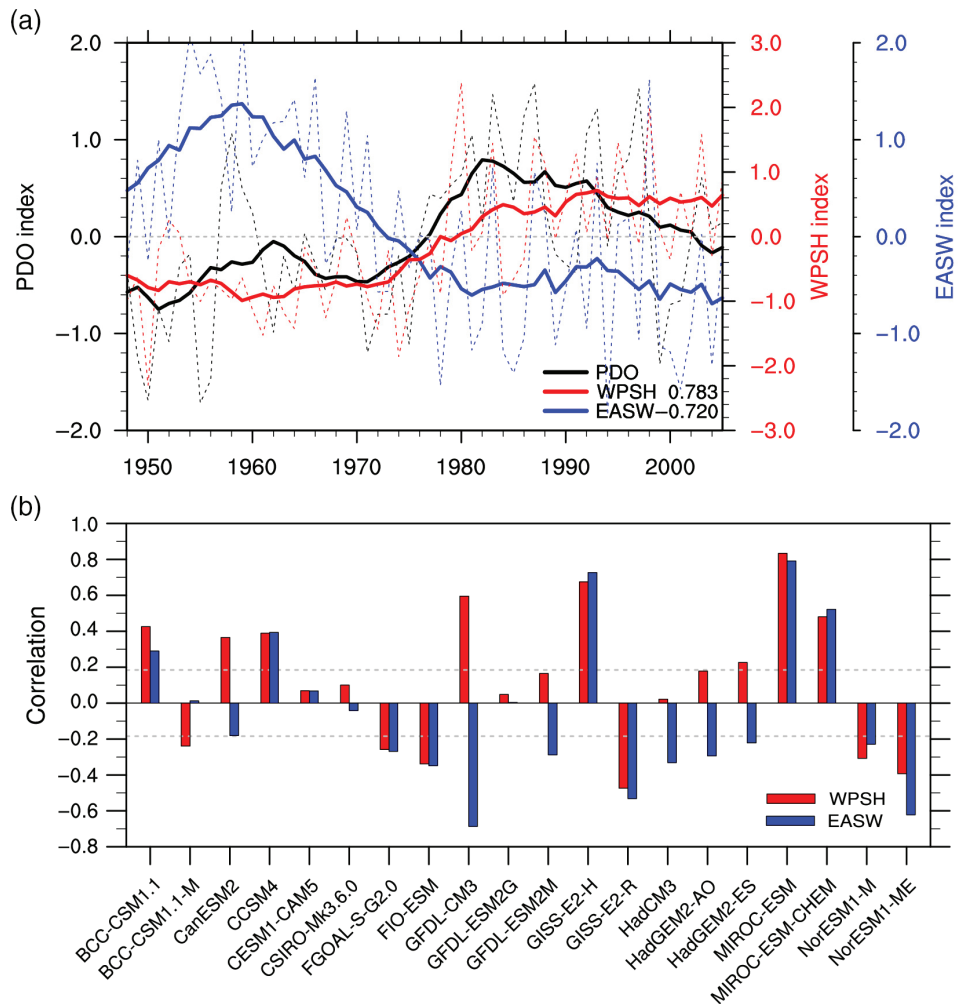


Figure 10. (a) Time series of the PDO, WPSH and EASW indexes (1948–2005). Thin (thick) lines represent the annual (11-year smoothed) PDO indexes for ERSST (black), the standardized WPSH and EASW indexes for NCEP/NCAR reanalysis data set. The numbers in the lower right corner represent the correlation between the PDO and WPSH/EASW index. (b) The correlation between the 11-year running mean of the PDO and the WPSH (red bars) and EASW (blue bars) from 1901–2005 in the 20 CMIP5 models is presented. The grey dashed line represents the correlation pass 95% confidence level.

the models capture the correlation between the winter precipitation over southern North America and the PDO, especially CCSM4, BCC-CSM1.1 and HadGEM2-ES (Figure 13). Except for GFDL-ESM2G, GISS-H-R, HadCM3, NorESM1-M and NorESM2-ME, most of the models captured the negative correlation between the 700 hPa geopotential height anomaly in southern North America region and the PDO (Figure 14), which may be the reason for the good performance of the models in simulating the correlation between the winter precipitation over southern North America and the PDO.

On the whole, the CMIP5 models are good at simulating the impact of the PDO on winter precipitation in southern North America but are less reliable for summer precipitation in eastern China. This is probably because the models are not good at simulating the positive/negative correlation between the PDO and the WPSH/EASW, but are better at capturing the negative 700 hPa geopotential height anomaly over southern North America region during the warm phases of the PDO.

## 5. Summary and discussion

Some recent studies (Newman *et al.*, 2012; Polade *et al.*, 2013; Yim *et al.*, 2015; Wang and Li, 2017) have indicated that the CMIP5 models are generally capable of simulating the spatial pattern of the PDO. Because the PDO has significant impacts on the atmosphere, ocean and marine ecosystems (Shan *et al.*, 2014), we provide the systematic assessment of PDO simulations from CMIP5 in this study. First, we have provided an overview of the global/regional SSTA over the 136 years of historical simulations from the CMIP5 models. The observed SSTA shows a warming trend in the North Indian Ocean, the equatorial Pacific and especially in the South Atlantic but shows a cooling trend in the high latitudes of the North Atlantic and Southern Hemisphere. The warming/cooling trends seen in ERSST are greater than those in COBE. Compared to the observations, the models are good at simulating the overall global warming, and the pattern correlations of the SSTA trends in 65% (13 of 20) of the models are above 0.8 when compared with ERSST. However, the SSTA trends in the North

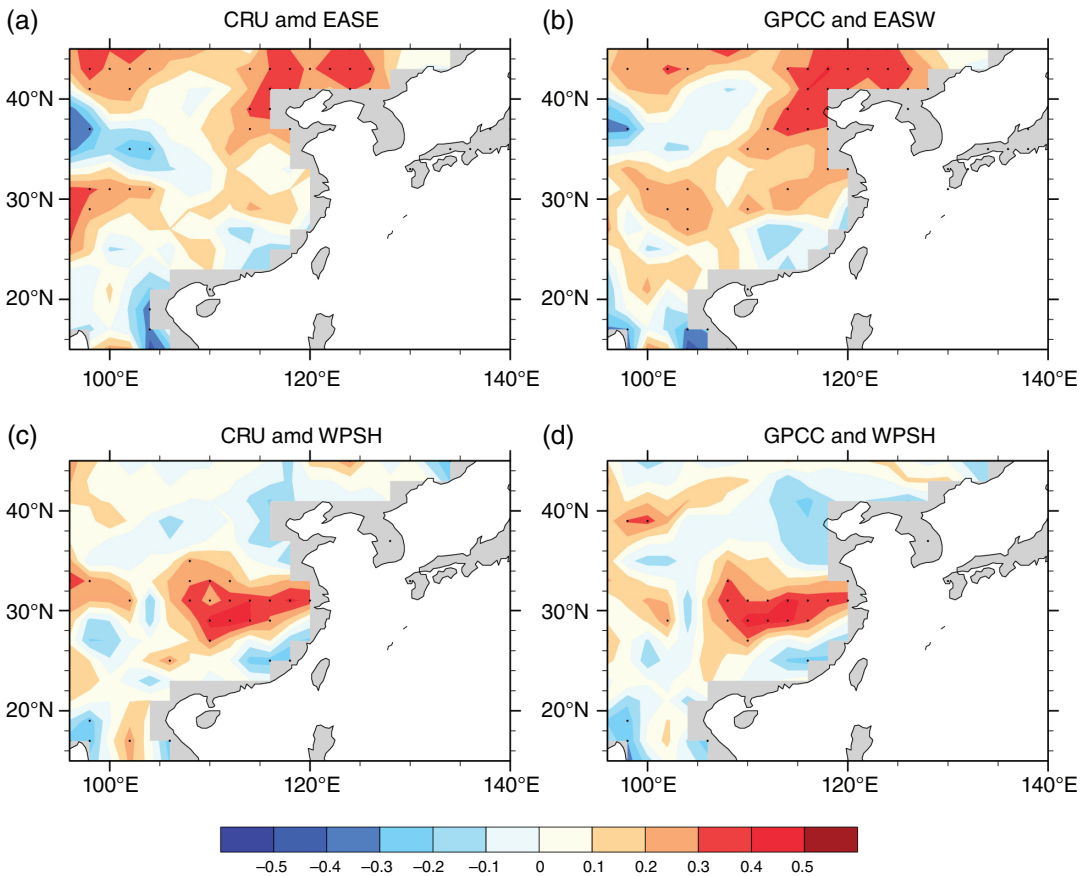


Figure 11. Spatial pattern of the correlation between the summer (JJA) precipitation anomaly over East Asia and EASW (a–b) and WPSH (c–d) index in the observations [CRU (left) and GPCC (right)]. Black dots indicate statistical significance at the 95% confidence level based on Student's *t*-test.

Pacific and Atlantic show considerable differences, especially for the SSTA in the PDO region.

There is good agreement between the spatial distributions of the SD of the detrended SSTA from ERSST and COBE. The SD of the detrended SSTA in the central and eastern tropical Pacific, North Pacific, North Atlantic and South Atlantic are relatively high, especially in the central and eastern equatorial Pacific, followed by that in the North Pacific. In terms of the CMIP5 models, some overestimate the warming/cooling trends, while some are similar to the observed trends but slightly smaller in magnitude. Most of the models overestimate the SD of the detrended SSTA in the North Pacific, North Atlantic and tropical central and eastern Pacific.

The globally averaged SSTA of the three observational data sets has consistent decadal variation. However, the globally averaged SSTA during 1900–1940 in CMIP5 EM and that in the observations show considerable divergence, and CMIP5 EM poorly captures the cooling trend of the SSTA before 1910. This is mainly due to the SSTA in the PDO and AMO regions among the five regions we chose, and the dominant signal is the SSTA in the PDO region. The SSTA in the Arctic Ocean simulated by the CMIP5 models is consistent with that in the ERSST. The results show that the interannual variabilities of the SSTA in the equatorial central and eastern Pacific regions and in the

tropical Indian Ocean are large, and CMIP5 EM does not simulate this interannual variability but does capture the warming trends in these two regions.

The PDO indexes in the observations show consistent decadal variations with main periods of 40–60 years, but only several models simulate the significant 40-year period of the PDO, including CESM1-CAM5, CSIRO-Mk3.6.0, GFDL-ESM2G, GISS-E2-R and MIROC-ESM-CHEM; the significant cycles of most other models had 60–80 year periods. The PDO indexes in the 20 models used here have random phases. In addition, the two best models for PDO index simulation are BCC-CSM1.1 and GFDL-ESM2G. For the spatial pattern of the PDO, the spatial pattern correlations are above 0.8 in all of the models, except in GISS-E2-H and GISS-E2-R; the best models for this purpose are HadGEM2-AO, CSIRO-Mk3.6.0 and GFDL-CM3. The climate models are better at resolving the PDO spatial pattern, and 90% of the spatial correlations between the models and observations of the PDO spatial pattern are above 0.8, but the most significant cycle of the PDO indexes in most models have a period of 60–80 years, which differs from the observed PDO period (40–60 years).

The spatial pattern of the correlation between the PDO index and the SSTA is similar to the PDO spatial pattern in the North Pacific. The models that are not good at

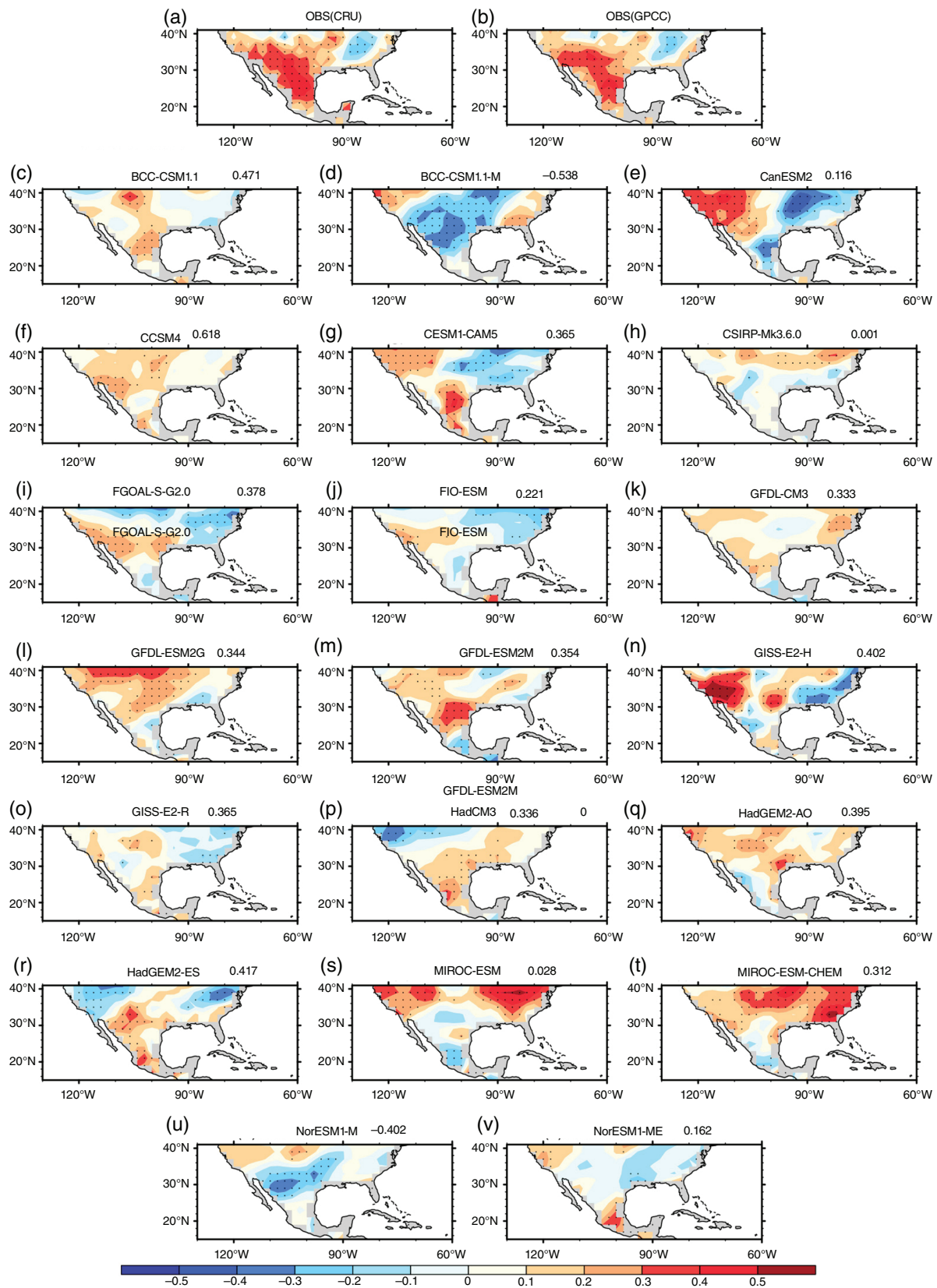


Figure 12. Spatial pattern of the correlation between 11-year running mean winter precipitation anomalies over southern North America (1901–2004) and the PDO index for the observations (CRU (a) and GPCC (b)) and models (c–v). The PDO indexes in a–b are from the ERSST data set, and the PDO indexes in c–v are from the respective model. Black dots indicate statistical significance at the 95% confidence level based on Student's *t*-test.

The spatial pattern correlation of the pattern in each model pattern and CRU is given in the right corner.

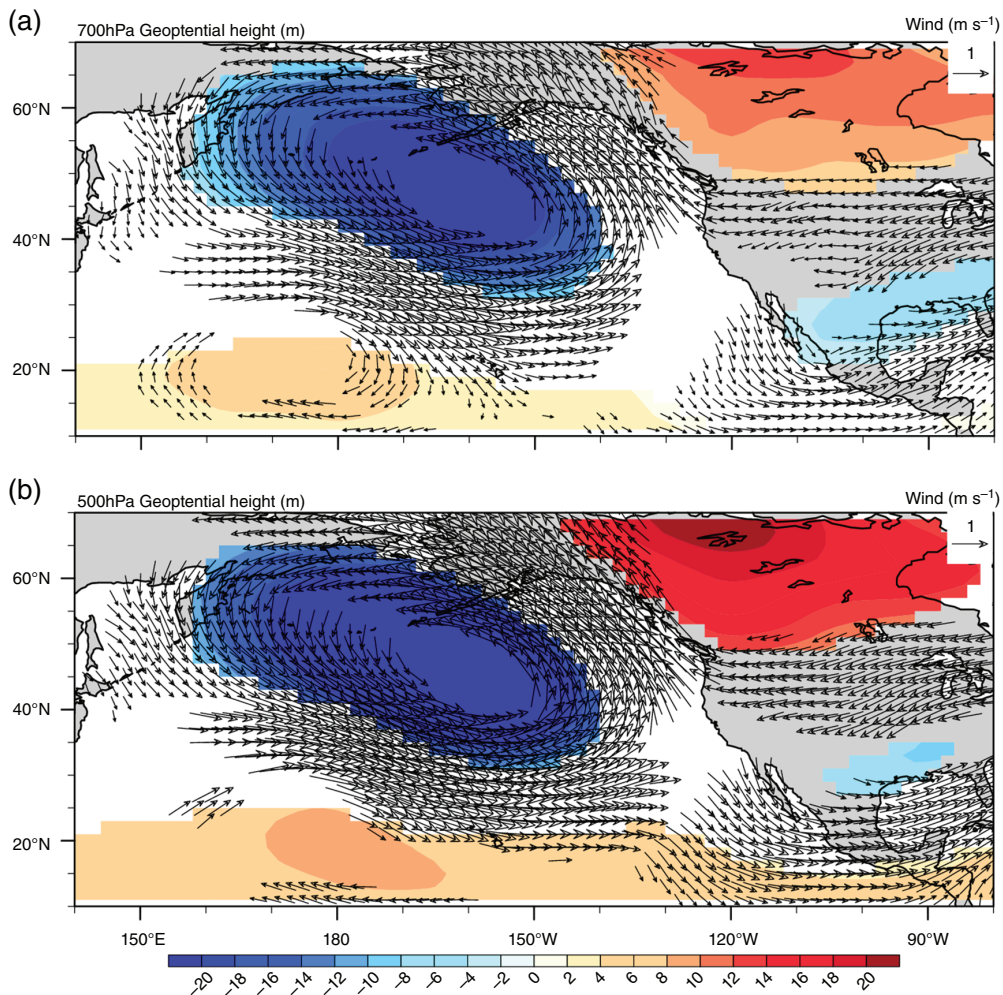


Figure 13. Regressions of the winter (DJF) geopotential height anomaly (colour shaded) and winds anomaly (contours) onto the PDO index from ERA20C (1948–2005) at (a) 700 hPa and (b) 500 hPa. Only anomalies with confidence levels exceeding 90% are plotted.

capturing the PDO spatial patterns are also not able to capture the correlation between the PDO index and the global SSTA. CCSM4, HadGEM2-ES and NorESM1-M are the most similar to the observations. In general, the models can simulate the basic correlation between the PDO and Pacific SSTA variability, but most of them overestimate the relationships in the Indian and Atlantic Oceans.

The PDO plays an important role in precipitation over eastern China and southern North America. Warm phases of the PDO tend to coincide with positive precipitation anomalies in the lower YRV and southern North America and negative anomalies in both North and South China (Figure 9). Some studies (He and Gong, 2002; Guo *et al.*, 2004; Verdon and Franks, 2006; Wang *et al.*, 2014b) have indicated that the PDO can influence the summer precipitation pattern over eastern China by influencing the WPSH and EASW. A strengthening west wind near the west coast of southern North America during the warm phases of the PDO is beneficial to water vapour transport to southern North America, leading to increased winter precipitation in the area. On the whole, the CMIP5 models are better at simulating the impact of the PDO on precipitation in southern North America but are less accurate for eastern

China. This is probably because most of the models cannot capture the impacts of the PDO on the WPSH and the EASW, but can simulate the negative geopotential height over the southern part of North America during the warm phases of the PDO.

In summary, CMIP5 is good at simulating the global SSTA trends but produces considerable differences over the North Pacific. Because the regional SSTA variabilities or errors are influenced by remote regions through teleconnections (Huang *et al.*, 1998), a better simulation of global mean SSTA does not mean a better simulation of regional SSTA (Wang *et al.*, 2014a). CMIP5 does not simulate the significant period or phase change of the PDO index, but it is better at simulating the PDO pattern and the spatial correlation pattern between the PDO index and global SSTA. This result indicates that CMIP5 models better simulate the relationship between the PDO area and global SSTA, but their ability to simulate SSTA variation in the PDO area is poor. In general, CMIP5 is not good at simulating decadal SSTA variability, and there is a considerable difference between the CMIP5 models. These results are of great significance for predicting future climate change and model improvement.

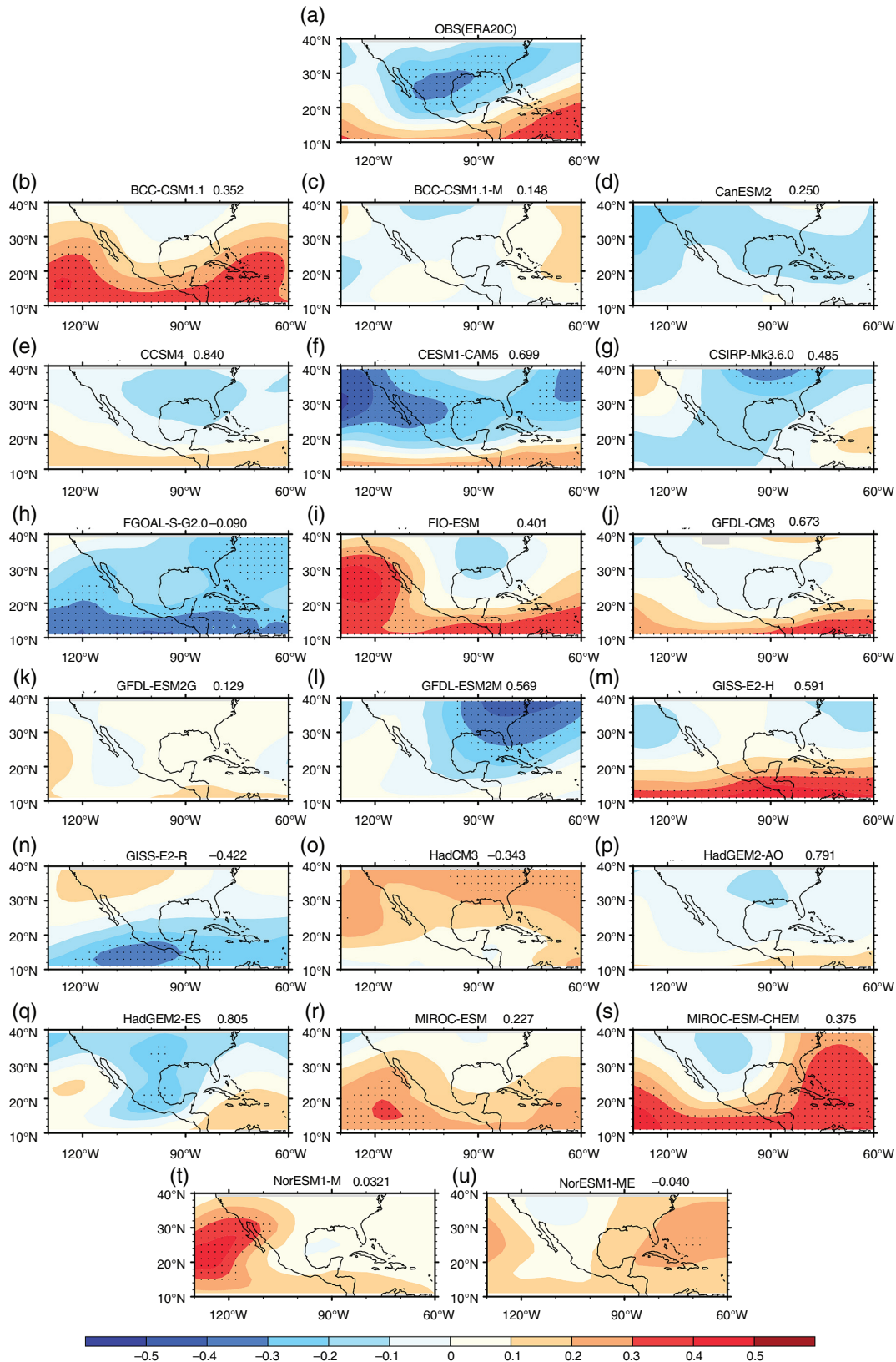


Figure 14. Spatial pattern of the correlation between the winter (DJF) 700 hPa geopotential height anomaly and the PDO index (1948–2004) for the observations (ERA20C (a)) and models (b–u). The PDO index in a is from the ERSST data set, and the PDO indexes in b–u are from the respective model. Black dots indicate statistical significance at the 95% confidence level based on Student's *t*-test. The spatial pattern correlation of the pattern in each model and ERA20C is given in the right corner.

## Acknowledgements

This work was jointly supported by the China Postdoctoral Science Foundation (2017M613250), the Natural Science Foundation of China (41705077, 41405003, and 41521004) and the Special Public Welfare Research Fund of China (GYHY201206009). The authors acknowledge the World Climate Research Programme's (WCRP) Working Group on Coupled Modelling (WGCM), the Global Organization for Earth System Science Portals (GO-ESSP) for producing the CMIP5 model simulations and making them available for analysis. The authors also acknowledge NOAA/OAR/ESRL PSD, Boulder, Colorado, USA, for providing NOAA\_ERSST\_V3b, COBE-SST2 data and GPCC precipitation data from their website at <https://www.esrl.noaa.gov/psd/>. More information about the data used in this study is available on the following website: CMIP5 model output (<http://cmip-pcmdi.llnl.gov/cmip5/>), SST from the Hadley Centre (HadSST3) (<http://www.metoffice.gov.uk/hadobs/hadsst3/>), the ERSST v3b and COBE-SST2 SST data and GPCC precipitation data (<https://www.esrl.noaa.gov/psd/data/gridded/>), and precipitation from CRU TS (<https://crudata.uea.ac.uk/cru/data/hrg/>), the US National Centers for Environmental Prediction/National Center for Atmospheric Research (NCEP/NCAR) (<https://www.esrl.noaa.gov/psd/>), and reanalysis data from ECMWF (<http://apps.ecmwf.int/datasets/>).

## References

- Allen RJ, Norris JR, Kovilakam M. 2014. Influence of anthropogenic aerosols and the Pacific Decadal Oscillation on tropical belt width. *Nat. Geosci.* **7**: 270–274.
- Barlow M, Nigam S, Berbery EH. 2001. ENSO, Pacific decadal variability, and U.S. summertime precipitation, drought, and stream flow. *J. Clim.* **14**: 2105–2128.
- Bhaskar J, ZZ H, Kumar A. 2014. SST and ENSO variability and change simulated in historical experiments of CMIP5 models. *Clim. Dyn.* **42**: 2113–2124.
- Brown DP, Comrie AC. 2004. A winter precipitation ‘dipole’ in the western United States associated with multidecadal ENSO variability. *Geophys. Res. Lett.* **31**(9): L09203.
- Cayan DR, Dettinger MD, Diaz HF, Graham NE. 1998. Decadal variability of precipitation over western North America. *J. Clim.* **11**(12): 3148–3166.
- Chan JCL, Zhou W. 2005. PDO, ENSO and the early summer monsoon rainfall over south China. *Geophys. Res. Lett.* **32**(8): 93–114.
- Chylek P, Dubey MK, Lesins G, Li J, Hengartner N. 2014. Imprint of the Atlantic multi-decadal oscillation and Pacific Decadal Oscillation on southwestern US climate: past, present, and future. *Clim. Dyn.* **43**(1–2): 119–129.
- Deser C, Phillips AS, Hurrell JW. 2004. Pacific interdecadal climate variability: linkages between the tropics and the North Pacific during boreal winter since 1900. *J. Clim.* **17**: 3109–3124.
- Deser C, Alexander MA, Xie S, Phillips AS. 2010. Sea surface temperature variability: patterns and mechanisms. *Annu. Rev. Mar. Sci.* **2**: 115–143.
- Ding Y, Wang Z, Sun Y. 2008. Inter-decadal variation of the summer precipitation in East China and its association with decreasing Asian summer monsoon. Part I: observed evidences. *Int. J. Climatol.* **28**(9): 1139–1161.
- Dong L, Zhou T. 2014a. The formation of the recent cooling in the eastern tropical Pacific Ocean and the associated climate impacts: a competition of global warming, IPO, and AMO. *J. Geophys. Res.* **119**: 11272–11287.
- Dong L, Zhou T. 2014b. The Indian Ocean sea surface temperature warming simulated by CMIP5 models during the twentieth century: competing forcing roles of GHGs and anthropogenic aerosols. *J. Clim.* **27**(9): 3348–3362.
- Dong L, Zhou T, Chen X. 2014. Changes of Pacific decadal variability in the twentieth century driven by internal variability, greenhouse gases, and aerosols. *Geophys. Res. Lett.* **41**: 8570–8577.
- Gershunov A, Barnett TP. 1998. Interdecadal modulation of ENSO teleconnections. *Bull. Am. Meteorol. Soc.* **79**: 2715–2725.
- Gong D, Ho CH. 2002. Shift in the summer rainfall over the Yangtze River valley in the late 1970s. *Geophys. Res. Lett.* **29**(10): 78–71.
- Guan X, Huang J, Guo R, Lin P. 2015a. The role of dynamically induced variability in the recent warming trend slowdown over the Northern Hemisphere. *Sci. Rep.* **5**: 12669.
- Guan X, Huang J, Guo R, Yu H, Lin P, Zhang Y. 2015b. Role of radiatively forced temperature changes in enhanced semi-arid warming in the cold season over East Asia. *Atmos. Chem. Phys.* **15**: 13777–13786.
- Guo Q, Cai J, Shao X et al. 2004. Studies on the variations of East-Asian summer monsoon during AD 1873~2000. *Chin. J. Atmos. Sci.* **28**(2): 206–215.
- Hamlington BD, Leben RR, Strassburg MW, Nerem RS, Kim KY. 2013. Contribution of the Pacific Decadal Oscillation to global mean sea level trends. *Geophys. Res. Lett.* **40**: 5171–5175.
- Han Z, Luo F, Li S, Gao Y, Furevik T, Svendsen L. 2016. Simulation by cmip5 models of the Atlantic multidecadal oscillation and its climate impacts. *Adv. Atmos. Sci.* **33**: 1329–1342.
- Harris I, Jones PD, Osborn TJ, Lister DH. 2014. Updated high-resolution grids of monthly climatic observations—the CRU TS. 10 dataset. *Int. J. Climatol.* **34**: 623–642.
- Hartmann DL, Klein Tank AM, Rusticucci M et al. 2013. Observations: atmosphere and surface. In *Climate Change 2013: The Physical Science Basis. Contribution of Working Group I to the Fifth Assessment Report of the Intergovernmental Panel on Climate Change*. Cambridge University Press: Cambridge, UK and New York, NY.
- He X, Gong D. 2002. Interdecadal change in Western Pacific subtropical high and climatic effects. *J. Geogr. Sci.* **12**(2): 79–86.
- Hu ZZ. 1997. Interdecadal variability of summer climate over East Asia and its association with 500 hPa height and global sea surface temperature. *J. Geophys. Res.* **102**(D16): 19403–19412.
- Hu K, Huang G, Zheng X, Xie S, Qu X, Du Y, Liu L. 2014. Interdecadal variations in ENSO influences on northwest Pacific-East Asian early summertime climate simulated in CMIP5 models. *J. Clim.* **27**: 5982–5998.
- Huang J, Higuchi K, Shabbar A. 1998. The relationship between the North Atlantic Oscillation and El Niño-Southern Oscillation. *Geophys. Res. Lett.* **25**(14): 2707–2710.
- Huang J, Yu H, Guan X, Wang G, Guo R. 2015. Accelerated dryland expansion under climate change. *Nat. Clim. Change* **6**(2): 166–172.
- Huang J, Xie Y, Guan X, Li D, Ji F. 2016. The dynamics of the warming hiatus over the Northern Hemisphere. *Clim. Dyn.* **48**: 429–446.
- Huang J, Yu H, Dai A, Wei Y, Kang L. 2017. Drylands face potential threat under 2°C global warming target. *Nat. Clim. Change* **7**(6): 417:422–417:422. <https://doi.org/10.1038/NCLIMATE3275>.
- Ishii M, Shouji A, Sugimoto S, Matsumoto T. 2005. Objective analyses of sea surface temperature and marine meteorological variables for the 20th century using ICOADS and the Kobe collection. *Int. J. Climatol.* **25**: 865–879.
- Ji M, Huang J, Xie Y, Liu J. 2015. Comparison of dryland climate change in observations and CMIP5 simulations. *Adv. Atmos. Sci.* **32**: 1565–1574.
- Kalnay E, Kanamitsu M, Kistler R, Collins W, Deaven D, Gandin L, Iredell M, Saha S, White G, Woollen J, Zhu Y, Leetmaa A, Reynolds R. 1996. The NCEP/NCAR 40-year reanalysis project. *Bull. Am. Meteorol. Soc.* **77**: 437–470.
- Kavvada A, Ruiz-Barradas A, Nigam S. 2013. AMO’s structure and climate footprint in observations and IPCC AR5 climate simulations. *Clim. Dyn.* **41**: 1345–1364.
- Kennedy JJ, Rayner NA, Smith RO, Parker DE, Saunby M. 2011. Reassessing biases and other uncertainties in sea surface temperature observations measured in situ since 1850: 2. Biases and homogenization. *J. Geophys. Res.* **116**: 811–840.
- Knutson TR, Zeng F, Wittenberg AT. 2013. Multimodel assessment of regional surface temperature trends: CMIP3 and CMIP5 twentieth-century simulations. *J. Clim.* **26**: 8709–8743.
- Kosaka Y, Xie S. 2013. Recent global-warming hiatus tied to equatorial Pacific surface cooling. *Nature* **501**: 403–407.
- Kumar A, Wang H, Wang W, Xue Y, Hu ZZ. 2013. Does knowing the oceanic PDO phase help predict the atmospheric anomalies in subsequent months? *J. Clim.* **26**(4): 1268–1285.
- Kurtzman D, Scanlon BR. 2007. El Niño-Southern Oscillation and Pacific Decadal Oscillation impacts on precipitation in the southern

- and central United States: evaluation of spatial distribution and predictions. *Water Resour. Res.* **43**(431): W10427.
- Lapp SL, Jacques JMS, Barrow EM, Sauchyn DJ. 2012. GCM projections for the Pacific Decadal Oscillation under greenhouse forcing for the early 21st century. *Int. J. Climatol.* **32**: 1423–1442.
- Ma Z. 2007. The interdecadal trend and shift of dry/wet over the central part of North China and their relationship to the Pacific Decadal Oscillation (PDO). *Sci. Bull.* **52**(15): 2130–2139.
- Macdonald GM, Case RA. 2005. Variations in the Pacific Decadal Oscillation over the past millennium. *Geophys. Res. Lett.* **32**: 93–114.
- Mantua NJ, Hare SR. 2002. The Pacific Decadal Oscillation. *J. Oceanogr.* **58**: 35–44.
- Mantua NJ, Hare SR, Zhang Y, Wallace JM, Francis RC. 1997. A Pacific interdecadal climate oscillation with impacts on salmon production. *Bull. Am. Meteorol. Soc.* **78**: 1069–1079.
- Molteni F, Farineti R, Kucharski F, Stockdale TN. 2017. Modulation of air-sea fluxes by extratropical planetary waves and its impact during the recent surface warming slowdown. *Geophys. Res. Lett.* **44**: 1494–1502.
- Newman M, Compo GP, Alexander MA. 2003. ENSO-forced variability of the Pacific Decadal Oscillation. *J. Clim.* **16**(23): 3853–3857.
- Newman M, Alexander MA, Ault TR, Cobb KM, Deser C, Lorenzo ED et al. 2012. The Pacific Decadal Oscillation, revisited. *J. Clim.* **29**: 4399–4427.
- Nidheesh AG, Lengaigne M, Vialard J, Izumo T, Unnikrishnan AS, Cassou C. 2017. Influence of ENSO on the Pacific Decadal Oscillation in CMIP models. *Clim. Dyn.* **49**(1–18): 3309–3326.
- Oshima K, Tanimoto Y. 2009. An evaluation of reproducibility of the Pacific Decadal Oscillation in the CMIP3 simulations. *J. Meteorol. Soc. Jpn.* **87**: 755–770.
- Park JH, An SI, Yeh SW, Schneider N. 2013. Quantitative assessment of the climate components driving the Pacific Decadal Oscillation in climate models. *Theor. Appl. Climatol.* **112**: 431–445.
- Polade SD, Gershunov A, Cayan DR, Dettinger MD, Pierce DW. 2013. Natural climate variability and teleconnections to precipitation over the Pacific-North American region in CMIP3 and CMIP5 models. *Geophys. Res. Lett.* **40**: 2296–2301.
- Schneider U, Becker A, Finger P, Meyer-Christoffer A, Rudolf B, Ziese M. 2015. *GPCC full data reanalysis version 7.0 at 1.0°: monthly land-surface precipitation from rain-gauges built on GTS-based and historic data*. [https://doi.org/10.5676/DWD\\_GPCC/FD\\_M\\_V7\\_100](https://doi.org/10.5676/DWD_GPCC/FD_M_V7_100).
- Shan H, Guan Y, Huang J. 2014. Surface air temperature patterns on a decadal scale in China using self-organizing map and their relationship to Indo-Pacific warm pool. *Int. J. Climatol.* **34**: 3752–3765.
- Shen C, Wang WC, Gong W et al. 2006. A Pacific Decadal Oscillation record since 1470 AD reconstructed from proxy data of summer rainfall over eastern China. *Geophys. Res. Lett.* **33**(3): L03702.
- Si D, Ding Y. 2016. Oceanic forcings of the interdecadal variability in East Asian summer rainfall. *J. Clim.* **29**(21): 7633–7649.
- Smith TM, Reynolds RW, Peterson TC, Lawrimore J. 2008. Improvements to NOAA's historical merged land-ocean surface temperature analysis (1880–2006). *J. Clim.* **21**: 2283–2296.
- Taylor KE. 2001. Summarizing multiple aspects of model performance in a single diagram. *J. Geophys. Res.* **106**: 7183–7192.
- Taylor KE, Stouffer RJ, Meehl GA. 2012. An overview of CMIP5 and the experiment design. *Bull. Am. Meteorol. Soc.* **93**: 485–498.
- Trenberth KE, Fasullo JT. 2013. An apparent hiatus in global warming? *Earth's Future* **1**: 19–32.
- Trenberth KE, Fasullo JT, Branstator G, Phillips AS. 2014. Seasonal aspects of the recent pause in surface warming. *Nat. Clim. Change* **4**: 911–916.
- Verdon DC, Franks SW. 2006. Long-term behaviour of ENSO: interactions with the PDO over the past 400 years inferred from paleoclimate records. *Geophys. Res. Lett.* **33**: 272–288.
- Wang H. 2002. The instability of the East Asian summer monsoon-ENSO relations. *Adv. Atmos. Sci.* **19**(1): 1–11.
- Wang J, Li C. 2017. Low-frequency variability and possible changes in the North Pacific simulated by CMIP5 models. *J. Meteorol. Soc. Jpn.* **95**: 199–211.
- Wang L, Chen W, Huang R. 2008. Interdecadal modulation of PDO on the impact of ENSO on the East Asian winter monsoon. *Geophys. Res. Lett.* **35**: 1–4.
- Wang H, Kumar A, Wang W, Xue Y. 2012a. Seasonality of the Pacific Decadal Oscillation. *J. Clim.* **25**(1): 25–38.
- Wang H, Kumar A, Wang W, Xue Y. 2012b. Influence of ENSO on Pacific decadal variability: an analysis based on the NCEP climate forecast system. *J. Clim.* **25**(18): 6136–6151.
- Wang C, Zhang L, SK LEE, Wu L, Mechoso CR. 2014a. A global perspective on CMIP5 climate model biases. *Nat. Clim. Change* **4**: 201–205.
- Wang S, Huang J, He Y, Guan Y. 2014b. Combined effects of the Pacific Decadal Oscillation and El Niño-Southern Oscillation on global land dry-wet changes. *Sci. Rep.* **4**: 6651–6651.
- Watanabe M, Shiogama H, Tatebe H, Hayashi M, Ishii M, Kimoto M. 2014. Contribution of natural decadal variability to global warming acceleration and hiatus. *Nat. Clim. Change* **4**: 893–897.
- Xie S, Du Y, Huang G, Zheng X, Tokinaga H, Hu K, Liu Q. 2010. Decadal shift in El Niño influences on indo-western Pacific and East Asian climate in the 1970s. *J. Climate* **23**: 3352–3368.
- Xie Y, Liu Y, Huang J. 2016. Overestimated arctic warming and underestimated Eurasia mid-latitude warming in cmip5 simulations. *Int. J. Climatol.* **36**: 4475–4487.
- Yang Q, Ma Z, Fan X et al. 2017. Decadal modulation of precipitation patterns over East China by sea surface temperature anomalies. *J. Clim.* **16**: 7017–7033.
- Yao S, Huang G, Wu R, Qu X. 2016. The global warming hiatus—a natural product of interactions of a secular warming trend and a multi-decadal oscillation. *Theor. Appl. Climatol.* **123**: 349–360.
- Yao S, Luo J, Huang G, Wang P. 2017. Distinct global warming rates tied to multiple ocean surface temperature changes. *Nat. Clim. Change* **7**: 486–491. <https://doi.org/10.1038/NCLIMATE3304>.
- Yim BY, Noh Y, Yeh SW, Kug JS, Min HS, Qiu B. 2013. Ocean mixed layer processes in the Pacific Decadal Oscillation in coupled general circulation models. *Clim. Dyn.* **41**: 1407–1417.
- Yim BY, Kwon MH, Hong SM, Kug JS. 2015. Pacific decadal oscillation and its relation to the extratropical atmospheric variation in cmip5. *Clim. Dyn.* **44**: 1521–1540.
- Yu L. 2013. Potential correlation between the decadal East Asian summer monsoon variability and the Pacific Decadal Oscillation. *Atmos. Oceanic Sci. Lett.* **6**(5): 394–397.
- Yu L, Furevik T, Otterå OH, Gao Y. 2015. Modulation of the Pacific Decadal Oscillation on the summer precipitation over East China: a comparison of observations to 600-years control run of Bergen climate model. *Clim. Dyn.* **44**: 475–494.
- Zhang L, Delworth TL. 2016. Simulated response of the Pacific decadal oscillation to climate change. *J. Clim.* **29**: 5999–6018.
- Zhang Y, Wallace JM, Battisti DS. 1997. ENSO-like interdecadal variability: 1900–1993. *J. Clim.* **10**(5): 1004–1020.
- Zhou T, Yu R. 2005. Atmospheric water vapor transport associated with typical anomalous summer rainfall patterns in China. *J. Geophys. Res.* **110**(8): 211–211.
- Zhou T, Gong D, Li J, Li B. 2009a. Detecting and understanding the multi-decadal variability of the East Asian summer monsoon—recent progress and state of affairs. *Meteorol. Z.* **18**(4): 455–467.
- Zhou T, Yu R, Jie Z et al. 2009b. Why the western Pacific subtropical high has extended westward since the late 1970s. *J. Clim.* **22**(8): 2199–2215.
- Zhu Y, Yang X. 2003. Relationships between Pacific Decadal Oscillation and climate variabilities in China. *Acta Meteor. Sin.* **61**(6): 641–654.
- Zhu Y, Wang H, Zhou W, Ma J. 2011. Recent changes in the summer precipitation pattern in East China and the background circulation. *Clim. Dyn.* **36**: 1463–1473.
- Zhu Y, Wang H, Ma J, Wang T, Sun J. 2015. Contribution of the phase transition of Pacific Decadal Oscillation to the late 1990s' shift in east China summer rainfall. *J. Geophys. Res.* **120**: 8817–8827.